Distributed acoustic sensing for near-surface imaging using submarine telecommunication cable: a case study in the Trondheimsfjord, Norway

Kittinat Taweesintananon*, Martin Landrø*, Jan Kristoffer Brenne† and Aksel Haukanes†

**Department of Electronic Systems, Faculty of Information Technology and Electrical Engineering, NTNU – Norwegian University of Science and Technology, Trondheim, Norway. E-mail: kittinat.taweesintananon@ntnu.no; martin.landro@ntnu.no.*

†*Alcatel Submarine Networks Norway AS, Vestre Rosten 77, Tiller, Norway. E-mail: jan.kristoffer.brenne@asn.com; aksel.haukanes@asn.com.*

(May 12, 2021)

GEO-2020-0834.R2

Running head: **DAS for near-surface imaging**

ABSTRACT

Distributed acoustic sensing (DAS) transforms submarine telecommunication cables into densely sampled seismic receivers. To demonstrate DAS applications for seismic imaging, we use an optical cable on the seafloor in the Trondheimsfjord, Norway, to record seismic data generated by a controlled seismic source. The data are simultaneously recorded by a towed hydrophone array and the fiber optic cable. Following our data processing methods, we can produce seismic images of the seafloor and underlying geological structures from both hydrophone array and DAS data. We find that the hydrophone and DAS data have a comparable signal-to-noise ratio. Moreover, DAS images can be improved by using a seismic

source that has sufficiently large energy within the frequency range matching the spatial resolution of DAS. The temporal resolution of the DAS images can be improved by minimizing the crossline offset between seismic sources and the DAS cable. The seismic images from DAS can be used to support geohazard analysis and various subsurface exploration activities.

INTRODUCTION

Near-surface seismic imaging is essential for investigating shallow gas, weak layers, faults, and other potential subsurface geological hazards. These elements can adversely affect offshore activities such as drilling operations, offshore platform and wind farm construction, and pipeline surveys. The oil and gas industry uses near-surface information to improve the images of deeper structures and to reduce risks in exploration and production. To accurately investigate near-surface irregularities, ultrahigh-resolution reflection seismic data acquisition and processing techniques have been developed (Monrigal et al., 2017).

Marine seismic data can be recorded either by hydrophone streamers towed behind sailing vessels or by seismic receivers deployed on the seafloor. Seismic reflections from near-surface structures are strongest at the receivers with short offsets from the source. To acquire near-offset seismic data, we may place the source over the streamer spread, which requires separate vessels for sources and streamers (Vinje et al., 2017). Another solution is to minimize the distance between sources and dense streamers (Thomas et al., 2012; Monrigal et al., 2017). However, the latter solution requires shortening the streamer length for operation safety. The lack of far offset information consequently causes high uncertainty in velocity model building. On the other hand, short offsets and dense receiver spacing in streamers result in high stacking fold and narrow imaging bins for near-surface imaging. Hence, when combined with high-frequency seismic sources, the vertical and horizontal resolution becomes significantly higher than conventional broadband seismic data.

Seabed seismic acquisition has been growing in the marine seismic market for its advantages over towed streamer techniques. The physics of seabed seismic acquisition is more advantageous than towed streamer acquisition for the following reasons (Landrø and

Amundsen, 2018). First, seafloor receivers have lower noise level than towed streamers. Second, there are no limits to the offsets and azimuths between sources and receivers, except for source-vessel considerations. Long offsets and wide azimuths in the data can significantly improve the accuracy of seismic velocity models and the seismic illumination of complex structures. Third, pressure and shear waves are both recorded, so a seafloor receiver geometry can provide high-quality images even in areas with strong amplitude absorption in the presence of gas. Finally, there are fewer effects from the sea surface ghosts that limit the frequency bandwidth of the seismic data and, hence, the image resolution.

Ocean bottom cables and ocean bottom nodes are common recording systems in the seabed seismic market. The node system is a blind recording system, as it acquires data internally and exports the data later. In addition, nodes are powered by internal batteries which requires an effective power management plan during the operation. In contrast, data recorded by ocean bottom cables can be viewed on a real-time basis. Traditional cable systems for seabed seismic acquisition are bulky electronic networks. However, the electrical cables can be replaced with fiber optic sensing cables, while maintaining the recording performance (Langhammer et al., 2010). In addition to the real-time monitoring feature, a key advantage of fiber optic sensing systems is that no electronic and electrical power components are required at the sensing points giving unsurpassed reliability for permanently installed sensing systems.

Distributed Acoustic Sensing (DAS) is an emerging technology that uses fiber optic cables for acoustic measurements. It has been applied to military defense, engineering structure monitoring and petroleum exploration (Wang et al., 2019). DAS transforms a fiber optic cable into a densely sampled sensor array. The cable itself is the sensing element without additional transducers in the optical path. Laser pulses transmitted into the fiber

are continuously reflected to the interrogator due to the Rayleigh backscattering process inherent to all optical fibers. The phase of the backscattered light is reconstructed within the interrogator typically for each meter of the fiber. As the phase of the reflected optical light is proportional to the strain of the fiber, the distributed strain modulation across a fiber segment (termed the gauge length) can be computed. Therefore, DAS can sense seismic waves that modulate the extensional strain of the fiber segment (Hartog, 2017). Its seismic response is somewhat similar to the inline component of conventional point accelerometers. In other words, it is mainly sensitive to seismic waves creating strain along the cable direction (Kuvshinov, 2016; Papp et al., 2017).

Over the past decade, many applications of DAS have been studied and introduced to the applied seismology community and the petroleum industry. Daley et al. (2013) demonstrate a field test of DAS seismic acquisition of borehole seismic data and land surface seismic data. Additionally, Dean et al. (2016) discuss its applications to marine seismic acquisition. Lumens (2014) studies various applications of DAS in oil and gas wells. In addition to borehole applications, DAS can be applied to fiber optic telecommunication cables deployed on the ground and seafloor. Many case studies of DAS using onshore telecommunication infrastructure have been conducted for passive seismic monitoring such as earthquake detection (Biondi et al., 2017; Ajo-Franklin et al., 2019; Yu et al., 2019; Fernández-Ruiz et al., 2020), near-surface soil studies (Dou et al., 2017; Fang et al., 2020), ambient noise analysis (Ajo-Franklin et al., 2015; Martin et al., 2017, 2018), urban traffic monitoring (Kowarik et al., 2020; Lindsey et al., 2020), glacier flow monitoring (Walter et al., 2020), and other seismic activities (Zhu et al., 2021). Moreover, it can monitor seismic waves from controlled sources to study and prevent onshore geohazards (Ajo-Franklin et al., 2017). In addition to onshore environments, DAS in underwater telecommunication fibers

can detect ocean waves, microseisms, earthquakes (Sladen et al., 2019; Williams et al., 2019), and near-surface geological structures and faults (Lindsey et al., 2019).

DAS can be used as surface seismic receivers in subsurface exploration. Bakulin et al. (2019) and Urosevic et al. (2019) demonstrate the potential applications of DAS to land seismic exploration. A comprehensive review of the recent DAS technology for land surface seismic surveys is given in Bakulin et al. (2020). Nevertheless, the applications of DAS to produce subsurface seismic images in a marine environment have not been widely presented. It is important to acquire multifold and diverse examples to verify that DAS can be used for subsurface seismic exploration in any environment. This statement could be demonstrated by comparing the marine seismic images from DAS with those from other conventional seismic methods. The validity of DAS in marine seismic exploration has the potential in the seabed seismic market.

This article demonstrates seabed seismic applications of DAS for near-surface seismic imaging. The experiment is done by using an existing submarine telecommunication cable in the Trondheimsfjord, Norway. We first use DAS to record seismic waves generated from a bubble gun towed near the sea surface. Then, we analyze and process the data to produce seismic images of the seafloor and its underlying geological structures. The results are, then, compared to the seismic data simultaneously recorded by a conventional towed hydrophone array. Finally, we discuss the requirements and limitations of DAS for seabed seismic acquisition and subsurface imaging.

EXPERIMENTAL SETUP AND DATA ACQUISITION

We conduct a marine seismic survey in the Trondheimsfjord using NTNU's research vessel, R/V Gunnerus, as shown in Figure 1. One single marine seismic source and one single-channel hydrophone streamer are towed behind the vessel. The seismic data from the streamer are recorded by HMS-620 Bubble Gun Recording System through Subbottom Sonar Interface Software from National Instrument. Simultaneously, we record the seismic data using an OptoDAS interrogator connected to a dark fiber in a seafloor telecommunication cable. The OptoDAS interrogator, which was developed by Alcatel Submarine Networks, is based on the use of linear frequency modulated optical pulses (Waagaard et al., 2021). The DAS data are continuously recorded throughout the survey program. The map of the source line and DAS cable is shown in Figure 2.

The seismic recording system of the vessel consists of HMS-620 Bubble Pulser electric seismic source and a short hydrophone streamer with 7 m of a single-channel array comprising 24 elements. The source and streamer are towed approximately 20 m behind the vessel's reference position, and they are separated by 10 m perpendicular to the sail line. The source and streamer depths are approximately 1 m below the sea surface. The recording time sampling interval is 0.25 ms, and the maximum recording time for each shot is 266.25 ms. The recording start time is synchronized with the gun firing time. The layout diagram of the source and streamer towed behind the vessel is shown in Figure 3.

The acoustic source energy is approximately 50 J, which is equivalent to 200 dB relative to the reference pressure 1 μPa at reference distance 1 m. The frequency bandwidth ranges from 350–1000 Hz at 10 dB down, where the dominant frequency is about 600 Hz. The shot time interval, namely gun firing time interval, is set to 267.75 ms in the system. Our

analysis shows that the actual shot time interval is slightly shorter than this value due to instrument errors. The actual shot time interval estimated by our calibration method is about 267.67 ms. The vessel is navigated to be as close to the DAS cable as possible. The vessel speed averages 2 knots to acquire high-density seismic data with minimal noise from the vessel's propulsion. Hence, the average shotpoint interval is approximately 0.275 m.

The DAS recording system is independent of the vessel's equipment. The OptoDAS interrogator is connected to one end of the telecommunication cable in Trondheim. The cable was already laid into the soft sediments at about 0–2 m below the seafloor of the Trondheimsfjord from Trondheim to Kvithylla. An SMF-28 single mode silica fiber in the cable is used in our experiment. The interrogation is performed by sending frequency swept light pulses into the sensing fiber. Then, the light pulses are backscattered at the inherent anomalies presented in the fiber due to Rayleigh backscattering. After receiving the backscattered pulses, the OptoDAS interrogator calculates the time differentiated phase change of the backscattered response from consecutive sweeps for each sampled fiber position. Thereafter, the recorded time differentiated phase change can be converted to the longitudinal strain of the corresponding fiber section. The DAS data are continuously recorded using 0.44 ms time sampling interval throughout the survey. The channel spacing is 2.04 m, while the gauge length is 4.08 m.

DAS recording system

In this experiment, we repeatedly send light pulses with a free-space wavelength (λ_o) of 1550 nm, in which the sampling period at the optical receiver ($\Delta\tau$) is 1×10^{-8} s. The

spatial sampling interval (SSI) is defined by the sampling period as

$$\mathrm{SSI} = \left(\frac{c}{2n_g}\right)\Delta\tau, \tag{1}$$

where $c \approx 3 \times 10^8$ m/s is the speed of light in vacuum, and $n_g \approx 1.47$ is the refractive group index of the SMF-28 fiber. Hence, SSI ≈ 1.02 m.

Let ϕ_x be the phase of the light backscattered from the spatial sampling location x, which can be expressed in radians as

$$\phi_x = \frac{4\pi n_g x}{\lambda_o}. \tag{2}$$

The interrogator extracts the rate of phase change between consecutive time samples associated with this location, namely, the time differentiated phase ($\dot{\phi}_x$). In this study, the time sampling interval (Δt) is 0.44 ms, which is defined by the cable length of 44 km. The SSI is decimated to the desired spatial resolution by applying a spatial moving average to the time differentiated phase ($\dot{\phi}_{\mathrm{avg},x}$) around the location x. In this experiment, the resolution is calculated by averaging across four spatial samples ($N_{\mathrm{avg}} = 4$) to achieve a full width at half maximum ($L_W = N_{\mathrm{avg}} \times \mathrm{SSI}$), i.e., $L_W \approx 4.08$ m. Then, the difference of the average time differentiated phases between the two spatial locations separated by four spatial samples ($N_{\Delta\tau} = 4$) is defined as the time differentiated phase change ($\Delta\dot{\phi}_x$):

$$\Delta\dot{\phi}_x = \dot{\phi}_{\mathrm{avg},x+L_G/2} - \dot{\phi}_{\mathrm{avg},x-L_G/2}, \tag{3}$$

where $L_G = N_{\Delta\tau} \times \mathrm{SSI}$ is the gauge length. Hence, $L_G \approx 4.08$ m. The gauge length is an acquisition parameter that affects the signal-to-noise ratio (S/N) and the spatial resolution of the raw DAS data (Dean et al., 2017).

The longitudinal strain rate ($\dot{\varepsilon}_{xx,x}$) of the fiber section can be derived from the time

differentiated phase change by

$$\dot{\varepsilon}_{xx,x} = \frac{\lambda_o}{4\pi n_g \zeta L_G} \Delta\dot{\phi}_x, \tag{4}$$

where ζ is the strain-optic coefficient described by

$$\zeta = 1 - \frac{n_g^2}{2} \left[P_{12} - \nu \left(P_{11} + P_{12} \right) \right], \tag{5}$$

and P_{11} and P_{12} are the Pockel photoelastic constants, and ν is Poisson's ratio of the fiber material (Bertholds and Dandliker, 1988; Hartog, 2017). In this experiment, we use $\zeta \approx 0.78$ for the silica fiber.

Thus, the longitudinal strain ($\varepsilon_{xx,x}$) of the fiber section can be determined by integrating the strain rate along the time axis, i.e.,

$$\varepsilon_{xx,x} = \int_0^t \dot{\varepsilon}_{xx,x} \, dt. \tag{6}$$

On the other hand, the maximum number of recording channels is given by $\Delta t / \Delta \tau$, which is 44000 channels along the cable length of 44 km. In this experiment, we extract only 10500 channels sampled at every 2.04 m from 0 to 21 km from the optical circulator for recording the time differentiated phase change data. The extracted subsections of the data are defined by regions of interest. In this case, the channel spacing is larger than SSI by a factor of two.

Strain-optic relation

Equation 4 can easily mislead. As a constant strain-optic coefficient is used, equation 4 implies that the time differentiated phase change is merely a function of the longitudinal deformation of the fiber. In fact, the strain-optic coefficient defined in equation 5 is implicitly

affected by both longitudinal and transverse deformations of the fiber. The phase of the light in radians is defined as

$$\phi = 2\pi \left(\frac{L_o}{\lambda_o} \right), \tag{7}$$

where L_o and λ_o are the optical path length and wavelength in free space, respectively. The optical path length is defined as

$$L_o = n_g L = \left(\frac{c}{v_{ph}} \right) L, \tag{8}$$

where c is the speed of light in vacuum, v_{ph} is the speed of light in the fiber, and L is the distance traveled by the light inside the zone where the interference effects are observed. Equation 8 also suggests that the change in the optical path length is caused by the changes of either the physical length of the fiber or the phase velocity of the light. The relative change of an optical path can be written as

$$\frac{\Delta L_o}{L_o} = \varepsilon_L - \frac{\Delta v_{ph}}{v_{ph}}, \tag{9}$$

where $\varepsilon_L = \Delta L / L$ is the fiber strain in the direction of the light propagation (Kuvshinov, 2016).

For backscattering measurement, two-way propagation of light along the fiber axis gives $L \approx 2x$. Here, we neglect the fiber birefringence and consider a linearly polarized beam. Thus, the optical strain is approximately equal to the longitudinal strain: $\varepsilon_L \approx \varepsilon_{xx} = \Delta x / x$. Moreover, we see from equation 7 that a phase change is fundamentally caused by an optical path change. Given light with constant wavelength, the phase change across the gauge length ($x = L_G$) can be written as a function of the optical path change below:

$$\Delta\phi = \frac{2\pi}{\lambda_o} \Delta L_o \approx \frac{4\pi n_g L_G}{\lambda_o} \left(\frac{\Delta L_o}{L_o} \right). \tag{10}$$

Because the phase velocity of light depends on the dielectric tensor of the fiber, equation 9 for a uniform and isotropic material can be described by the Pockel constants as follows (Bakku, 2015; Kuvshinov, 2016).

$$\frac{\Delta L_o}{L_o} = \varepsilon_{xx} - \frac{n_g^2}{2}\left[\left(P_{11} - P_{44}\right)\varepsilon_\perp + P_{12}\varepsilon_{xx}\right], \tag{11}$$

where $\varepsilon_\perp$ is the transverse fiber strain, and $P_{12} = P_{11} - 2P_{44}$. For the parameters given by Kuvshinov (2016), equation 11 reduces to

$$\frac{\Delta L_o}{L_o} \approx 0.7\varepsilon_{xx} - 0.2\varepsilon_\perp. \tag{12}$$

This equation implies that the DAS signal based on a phase change method results from the strains in any direction.

For very small transverse stress ($\sigma_\perp \to 0$), the transverse fiber strain depends on the longitudinal strain by the Poisson effect (Kuvshinov, 2016):

$$\varepsilon_\perp = \varepsilon_{\perp,1} + \varepsilon_{\perp,2} \approx -2\nu\varepsilon_{xx}. \tag{13}$$

Then, the relative change of the optical path in a fiber is proportional to the physical longitudinal strain, i.e.,

$$\frac{\Delta L_o}{L_o} \approx \zeta\varepsilon_{xx}. \tag{14}$$

In this limit, the optical phase change is proportional to the longitudinal strain as described by equation 4. The linear relationship in equation 14 is currently the commonly accepted expression for the length change. It is also the basis of all practical DAS applications, while equation 12 is not widely adopted.

DATA CHARACTERISTICS

The seismic data recorded by the single-channel streamer can be displayed as a common channel gather as shown in Figure 4. The data are formed by summing a linear array of 24 hydrophone elements within 7 m streamer length into one recording channel. The data contain direct and reflected P waves. The direct wave as marked by "A" does not propagate through the subsurface. Therefore, only the reflected waves are used to image the seafloor and subsurface geological structures. In Figure 4, two strong seismic reflections are observed: the seafloor reflection as marked by "B", and crystalline bedrock reflection as marked by "C". The stratigraphy between the seafloor and the bedrock should be divided into two units as described by L'Heureux et al. (2009). The lower unit comprises deposits of Allerød and Younger Dryas age overlying bedrock. The upper unit comprises Holocene deposits of bioturbated clay, silty and sandy sediments, and it is overlain by poorly sorted sand with anthropogenic drops at the seafloor. However, the base Holocene reflection is not clearly observed in our data.

On the other hand, the DAS data are continuously recorded. Each seismic trace corresponds to an individual recording channel resulting from the strain demodulation across a fiber segment of 4 m gauge length, where the channel spacing is 2 m. To derive shot records for further analysis, every continuously recorded seismic trace is edited and broken into several shorter traces associated with different shot numbers. This trace editing requires the precise gun firing time of each shot, which is determined by the calibration method discussed in the next section.

Typical seismic profiles derived from DAS contain obvious hyperbolic events generated by our seismic sources. The data also contain low-frequency signals, as shown in Figure 5a,

that might include surface waves. However, our study focuses on the direct and reflected P waves, because the other source-generated waves like surface waves and converted waves are incomparable to the streamer data. A simple band-pass filter (160–960 Hz) can attenuate most of the undesired low-frequency contents and reveal the seismic signal directly propagating from the source as shown in Figure 5b. The direct wave is presented as a hyperbola on at least 40 recording channels (approximately 80 m of the cable). Reflected waves are barely observable in the shot profile, even after filtering. However, they can be enhanced and observed after supergathering as discussed later. Because the DAS receivers are trenched into the seafloor, the direct wave can be used to image the seafloor topography. The waves reflected from the subsurface below the seafloor are used to image the subsurface geological structures.

Seismic response of DAS in straight fiber

To demonstrate the seismic response of DAS to the direct P wave, we analyze both source directivity and receiver response. We assume that our source size is much smaller than the wavelength, such that the far field from a point source can be used. Due to spherical divergence, the amplitude of the seismic wave traveling from a point source to a receiver decreases linearly with the travel distance (r). Moreover, we consider the effect of source ghost on the propagating wavefield. The directivity of a harmonic source and its ghost can be combined with the spherical divergence to describe the propagating strain field as follows:

$$\varepsilon_{rr} = \frac{1}{r}\left[2\sin\left(\frac{2\pi f z_s}{v}\cos\phi\right)\right]\varepsilon_{\text{source}}, \tag{15}$$

where $\varepsilon_{\text{source}}$ is the strain field of frequency f generated by the seismic source at the depth z_s, v is the wave velocity in the water, and ϕ is the angle between the wave propagating

direction and the vertical axis as in Figure 6 (Drijkoningen, 2003). For the source depth $z_s = 0.60$ m and the velocity $v = 1490$ m/s, the directivity of the source with ghost associated with the square bracket in equation 15 is illustrated in Figure 7.

P waves generate strains parallel to the direction of the wave propagation. The impinging seismic waves, hence, induce strains in the cable, which are also transported from the buffer layer to the fiber core. Suppose a planar P wave propagates along the r-axis which forms the grazing angle θ with the straight cable along the x-axis as shown in Figure 6. The only non-zero strain component carried by the wave is ε_{rr}. Therefore, the projection of this strain component onto the cable axis is equal to

$$\varepsilon_{xx}^{(c)} = \varepsilon_{rr} \cos^2 \theta. \tag{16}$$

On the other hand, the projection onto the normal axis to the cable is equal to

$$\varepsilon_{\perp}^{(c)} = \varepsilon_{rr} \sin^2 \theta. \tag{17}$$

We now consider the anisotropic physical properties of a straight optical fiber embedded in a cable (elastic filler) as discussed by Kuvshinov (2016). Assuming that the fiber is perfectly coupled to the cable, the longitudinal deformation of both cable and fiber in response to longitudinal forces forms the isostrain loading condition. That is, the longitudinal strain ε_{xx} is transported from the cable to the fiber without losses:

$$\varepsilon_{xx}^{(f)} = \varepsilon_{xx}^{(c)}, \tag{18}$$

where the superscripts (f) and (c) denote the fiber and cable, respectively. On the other hand, the forces perpendicular to the cable axis with perfect coupling form the isostress loading condition, i.e., $\sigma_{\perp}^{(f)} = \sigma_{\perp}^{(c)}$. Hence, the transverse strain of the fiber is equal to the

transverse strain of the cable multiplied by the ratio of effective Young's modulus of the cable ($E^{(c)}$) to effective Young's modulus of the fiber ($E^{(f)}$):

$$\varepsilon_{\perp}^{(f)} = \left(\frac{E^{(c)}}{E^{(f)}}\right)\varepsilon_{\perp}^{(c)} \equiv \alpha\varepsilon_{\perp}^{(c)}, \tag{19}$$

where α is referred to as the ratio $E^{(c)}/E^{(f)}$ implying the efficiency of the transverse strain transfer from a cable to the embedded fiber. The coupling coefficient α becomes one, when the cable and fiber are made from the same material. However, the layered materials of the cable surrounding the fiber usually have smaller effective Young's modulus than the fiber core.

Using equation 12 and the definitions of fiber strains discussed above, we find that the relative change of an optical path in DAS varies with the grazing angle as

$$\frac{\Delta L_o}{L_o} \approx 0.7\varepsilon_{xx}^{(f)} - 0.2\varepsilon_{\perp}^{(f)} = \left(0.7\cos^2\theta - 0.2\alpha\sin^2\theta\right)\varepsilon_{rr}. \tag{20}$$

Figure 8 shows the responses of mapping the propagating strain field onto the optical path change as defined in the parenthesis in equation 20 with different coupling coefficients (α). For nonzero coupling coefficients, this expression implies that the P-wave amplitudes become a small negative value (reverse polarity) when the grazing angle is near 90°. This agrees with the measurement done by Papp et al. (2017). It also supports our observation in Figure 5b that the amplitude of the direct P wave does not fade towards the zero inline offset. Nevertheless, many studies assume that the effective Young's modulus of the cable materials is much smaller than the fiber ($\alpha \to 0$), so that the contribution of the transverse strain to the optical path change is negligible. Then, the optical path change is dominated by the $\cos^2\theta$ function (Mateeva et al., 2014; Kuvshinov, 2016). Therefore, they conclude that a P wave arriving with an angle close to 90° will be poorly detected using DAS in a straight fiber.

The uses of the spatial moving average and the spatial phase change defined by gauge length form two field arrays for a recording channel of DAS. The recorded signal (A_{DAS}) is the average strain at each sensing element. The average strain at a DAS channel is related to the point strain, i.e., the optical path change, through the combined array response below:

$$A_{\mathrm{DAS}} = \left[\frac{\sin\left(\frac{k_x L_G}{2}\right)}{\frac{k_x L_G}{2}}\right]\left[\frac{\sin\left(\frac{k_x L_W}{2}\right)}{\frac{k_x L_W}{2}}\right]\left(\frac{\Delta L_o}{L_o}\right), \tag{21}$$

where k_x is the angular wavenumber along the fiber axis, L_G is the gauge length, and L_W is the pulse width (Bakulin et al., 2020). Given the grazing angle θ, we obtain $k_x = k\cos\theta = (2\pi f/v)\cos\theta$. Therefore, equation 21 can be rewritten as

$$A_{\mathrm{DAS}} = \left[\frac{\sin\left(\frac{\pi f L_G}{v}\cos\theta\right)}{\frac{\pi f L_G}{v}\cos\theta}\right]\left[\frac{\sin\left(\frac{\pi f L_W}{v}\cos\theta\right)}{\frac{\pi f L_W}{v}\cos\theta}\right]\left(\frac{\Delta L_o}{L_o}\right), \tag{22}$$

where f and v are the frequency and velocity of the wave, respectively. Figure 9 shows the variation of the DAS array response with the frequency and velocity of the wave propagating in the same direction as the fiber axis ($\theta = 0$). On the other hand, Figure 10 shows its variation with the frequency and grazing angle of the wave in the water, where $v = 1490$ m/s. In this experiment, we use $L_G = L_W = 4.08$ m. The combined response of the point strain response in equation 20 and the DAS array response in equation 22 are the product of the two responses. This product contributes to the total DAS receiver array response as illustrated in Figure 11.

Combining the response of both source and receiver arrays from equations 15, 20, and 22,

we obtain the total directivity of the DAS system for a marine seismic survey as follows:

$$
\begin{aligned}
A_{\mathrm{DAS}} \approx & \left[\frac{\sin\left(\frac{\pi f L_G}{v}\cos\theta\right)}{\frac{\pi f L_G}{v}\cos\theta}\right]\left[\frac{\sin\left(\frac{\pi f L_W}{v}\cos\theta\right)}{\frac{\pi f L_W}{v}\cos\theta}\right] \\
& \times \left(0.7\cos^2\theta - 0.2\alpha\sin^2\theta\right) \\
& \times \frac{1}{r}\left[2\sin\left(\frac{2\pi f z_s}{v}\cos\phi\right)\right]\varepsilon_{\mathrm{source}}.
\end{aligned}
\tag{23}
$$

We can further rearrange equation 23 to determine the DAS amplitude variation with the receiver depth z and the inline offset h_x at different crossline offsets h_y. Here, $d = \sqrt{z^2 + h_y^2}$, $r = \sqrt{h_x^2 + d^2}$, $h = \sqrt{h_x^2 + h_y^2}$, $\theta = \arctan\left(d/h_x\right)$, and $\phi = \arctan\left(h/z\right)$. For a wave frequency at 600 Hz and perfect coupling in the DAS cable ($\alpha = 1$), Figures 12 and 13 show different relative amplitude responses of DAS to the direct P wave generated from a marine point source at 0.6 m depth, where the crossline offsets are 0 and 60 m, respectively. The amplitude responses at key water depths are also plotted at the bottom of each corresponding figure for clarity. For a wave with 600 Hz frequency and 1490 m/s velocity, we observe that the DAS receiver response negatively boosts the DAS amplitude at small inline offsets as shown in Figures 12b and 13b. On the other hand, it reduces the negative amplitude response at large inline offsets, where the response is a positive side lobe. This variation is also observed in the total response of the combined source and DAS arrays in Figures 12c and 13c.

We now consider the DAS amplitude response corresponding to the shot number 951 at the position of 2546 m as shown in Figure 5. At this position, the water depth is about 20 m, and the crossline offset is about 60 m as shown later in Figure 18. Figure 13c illustrates that the direct P wave from this source position is presented at small inline offsets in the DAS data. The amplitude should fade towards the larger offsets until about 40 m inline offset, at which the amplitude begins changing to the opposite polarity. At larger offsets,

the amplitude continues in this reverse polarity and tends to increase gently with offsets.

Thanks to the reciprocity relation of source and receiver, we can also observe this amplitude variation in a common receiver gather from channel number 1251 at position of 2555 m as plotted in Figure 14. Here, all of the seismic traces are associated with the same seabed condition at the receiver. Since the source signal is approximately identical for all the shots, the amplitude variation of the direct wave in this receiver gather mainly depends on the propagation angle of the wave. In Figure 14b, we observe the polarity flips of the direct wave at the inline offsets of -47 m and 56 m as marked by green arrows. The inline offsets where polarity flips occur are about 10 m larger than our estimate from Figure 13c. The discrepancy could result from the uncertainty of the source depth, wave frequency, velocity, and coupling coefficient parameters used in our calculation. The actual source depth depends on the sea state, while the actual wave is a multi-frequency wave pulse. Moreover, the actual P-wave velocity of the media around the fiber may be higher than the velocity in the water used in our calculation. It is also difficult to determine a precise critical offset from the real data, since this is the point where various types of waves including reflection, refraction, direct wave and surface wave are juxtaposed. Because the amplitude of the direct P wave in DAS is very small at this point, all the other waves become dominant. Despite some deviations, our observations are generally described by equation 23.

Note that the amplitude response based on equation 23 depends on several factors including the dominant frequency of the signal being recorded, and the physical properties of the telecommunication cable. This equation gives a possible explanation for the amplitude characteristics observed in our DAS data generated from a high-frequency seismic source. It is beyond the scope of this article to precisely determine the parameters, especially the coupling coefficient α, contributing to the amplitude response. For the further analysis in

this article, we focus on the methods to produce subsurface images, for which the coupling between impinging seismic waves and the DAS recorded signals is irrelevant.

METHODS

As a key reference, the seismic image of the seafloor and the subsurface from the single-channel streamer data is obtained through the following processes:

1. Apply a static time shift to redatum the source and receiver to the sea surface.
2. Apply Normal Move Out (NMO) correction to correct the traveltime from arbitrary offsets to zero offset, where the source and receiver are virtually at the same position. To be compared with the DAS data set, the NMO velocity from DAS data processing is used.
3. Mute the undesired direct wave.
4. Apply zero-offset time migration using the NMO velocity.

We also resample the streamer seismic data from 0.25 ms to 0.44 ms to match the time sampling interval of the DAS data.

Calibration of DAS seismic data

In contrast to streamer data, DAS data are continuously recorded along the cable with many more recording channels. To extract a shot profile from this continuously recorded data, we need to know the precise gun firing time of the source. However, it is our limitation that synchronous sampling of the DAS and streamer recording systems was not used in our experiment. Therefore, we use the coordinated universal time (UTC) time stamps of the

gun firing from the recorded streamer data to tailor the continuously recorded DAS data into several shot profiles. Unfortunately, the streamer data are recorded in SEG-Y format, in which the time stamps are stored at the accuracy of 1 s only. In contrast, the recording time interval of the DAS data is 0.44 ms. Therefore, it is uncertain to define the exact time sample in the DAS data when the gun is fired from the given time stamp with lower precision. To overcome this challenge, we propose a data-driven method to estimate the start time of each shot record from the corresponding first arrival time in our DAS data.

Assuming the DAS receivers are on the seafloor, the first arrival event at near offsets is the direct wave propagating from the source to DAS receivers as shown in Figure 6. Given time picks of the first arrival at the inline offset of $h_x = 0$ and any h_x, we can estimate the source-to-cable distance (d) and, then, the start UTC time of a DAS shot record (t_0) using the following expressions (see Appendix A for derivation):

$$d = \frac{v}{2\Delta\tau}\left(\frac{h_x^2}{v^2} - (\Delta\tau)^2\right), \tag{24}$$

and

$$t_0 = t_{\{h_x=0\}} - \tau_{\{h_x=0\}} = t_{\{h_x=0\}} - \frac{d}{v}, \tag{25}$$

where v is the P-wave velocity in the sea water, t is the picked UTC time at which the direct wave arrives at a receiver on the DAS cable, τ is the traveltime for the wave that propagates directly from the source to a receiver, and $\Delta\tau$ is the difference between τ at $h_x = 0$ and τ at any h_x. That is, $\Delta\tau = \tau_{\{h_x\}} - \tau_{\{h_x=0\}}$, where $\tau_{\{h_x=0\}} = \frac{d}{v}$ by definition. In this study, we assume the velocity in water to be constant at 1490 m/s. Using the expressions above, we can derive the start UTC time of every shot and construct individual shot profiles of DAS.

It should be noted that equation 24 can determine the distance (d) between source and

DAS cable, even if no information of the source position is given. Consequently, equation 25 requires no source parameter to determine the gun firing time. Using this method, we find that the actual gun firing time interval is slightly shorter than the value we set to the shooting box. Moreover, given the water depth (z) of a receiver, we can estimate the crossline offset (h_y) using the expression below,

$$h_y = \sqrt{d^2 - z^2}. \tag{26}$$

Therefore, with sufficient constraints from the recording geometry, it is possible to derive the positions and time of sources from DAS data by analyzing the traveltime of the direct wave. Then, we may use the signals from unknown sources for subsurface imaging, which should be studied further. Nevertheless, this article will focus on the DAS application using controlled seismic sources. Even if there are no time synchronization issues in the survey, our proposed method can still be used to calibrate the positions and times of the seismic sources.

DAS seismic processing

Given shot profiles recorded by DAS, we do preconditioning steps to enhance the S/N of the data followed by imaging steps. Since the receivers are located at the seafloor, the seismic images of the seafloor and its underlying subsurface structures are generated from different seismic events. The seafloor image, i.e., water depth topography, can be derived from the direct wave from source to the receivers on the seafloor. On the other hand, the structural image below the seafloor can be derived from the corresponding seismic reflections. Hence, we require two different imaging methods to generate the complete subsurface image comprising both seafloor topography and its underlying structures. The

processing sequence for DAS data is summarized in Appendix B.

NMO correction for direct wave

The direct wave from the source to the DAS receivers on the seafloor is illustrated in Figure 15. The NMO traveltime correction ($\Delta t_{\mathrm{NMO,direct}}$) is to map the traveltime (t_{direct}) of the direct wave event to t_z, which is the one-way traveltime for the vertical propagation distance of z. The NMO correction for the direct wave is

$$\Delta t_{\mathrm{NMO,direct}} \equiv t_{\mathrm{direct}} - t_z = \sqrt{t_z^2 + \frac{h^2}{v^2}} - t_z, \tag{27}$$

where $t_{\mathrm{direct}} = \sqrt{t_z^2 + \frac{h^2}{v^2}}$, $h \equiv \sqrt{h_x^2 + h_y^2}$, $h_y = \sqrt{d^2 - z^2}$, and z is the known water depth for the central receiver ($h_x = 0$). Thus, the correction will produce the one-way-time zero-offset seismic gather where the source is virtually right above the central receiver. Multiplying the time axis by two will convert the gather into two-way time to be comparable with the seismic reflection data from the streamer.

In practice, we redatum the source and receivers to be at the sea surface prior to NMO correction to output the two-way traveltime seismic image. That is, the receiver static correction of t_z is added to the traveltime of the wave path in Figure 15a. Then, the traveltime of the shot profile after redatuming to the sea surface is defined as:

$$T_{\mathrm{direct}} \equiv t_{\mathrm{direct}} + t_z, \tag{28}$$

where t_{direct} is the one-way traveltime of direct wave from source to a receiver. Here, the NMO correction is to map the redatumed traveltime T_{direct} into the two-way traveltime for the vertical propagation distance from source to the seafloor, i.e.,

$$T_z = 2t_z. \tag{29}$$

Hence, the NMO correction for the direct wave after redatumed to the sea surface is

$$\Delta T_{\mathrm{NMO,direct}} \equiv T_{\mathrm{direct}} - T_z = t_{\mathrm{direct}} - t_z = \Delta t_{\mathrm{NMO,direct}}. \tag{30}$$

Using equations 27 and 29, we can explicitly derive the NMO correction for redatumed traveltime of direct wave in equation 30 as follows:

$$\Delta T_{\mathrm{NMO,direct}} = T_{\mathrm{direct}} - T_z = \sqrt{\frac{T_z^2}{4} + \frac{h^2}{v^2}} - \frac{T_z}{2}. \tag{31}$$

NMO correction for reflected wave

After redatuming source and receivers to the sea surface, we can apply a conventional NMO correction to the reflected wave. The NMO correction for the two-way traveltime of reflected wave can be written as follows:

$$\Delta T_{\mathrm{NMO,reflected}} = T_{\mathrm{reflected}} - T_z = \sqrt{T_z^2 + \frac{h^2}{v_{\mathrm{rms}}^2}} - T_z, \tag{32}$$

where $T_{\mathrm{reflected}}$ is the two-way traveltime of the reflected wave to the virtual receiver at the sea surface, T_z is the two-way traveltime for the vertical propagation distance from source to the reflector, and v_{rms} is the root-mean-square (RMS) velocity from the sea surface to the reflector. Velocity analysis is required to estimate proper velocities for different reflectors.

When the NMO correction for the direct wave using equation 31 is applied, the direct wave becomes flat in the common shot gather; however, all the subsurface reflections below the seafloor are overcorrected. On the other hand, the reflections will become flat if the NMO correction for reflected wave in equation 32 is applied using the proper velocity. However, the direct wave would then be undercorrected.

NMO stretch

NMO correction causes an inevitable frequency distortion, namely NMO stretching, especially for shallow events and at large offsets. As a result of stretching, seismic events are shifted to lower frequencies. The wavelet with a dominant period τ is stretched such that its period after NMO correction becomes τ_{NMO}, which is greater than τ by $\Delta\tau_{\text{NMO}}$. That is,

$$\tau_{\text{NMO}} = \tau + \Delta\tau_{\text{NMO}}. \tag{33}$$

Stretching is quantified by the change in the period of the wavelet divided by the initial dominant period, i.e., $\Delta\tau_{\text{NMO}}/\tau$. Hence, stretching for direct wave NMO correction for $\tau \ll T_z$ is quantified by

$$\frac{\Delta\tau_{\text{NMO,direct}}}{\tau} \approx \frac{\Delta T_{\text{NMO,direct}}}{T_z + \Delta T_{\text{NMO,direct}}}, \tag{34}$$

where T_z is the two-way traveltime for the vertical propagation distance from source to the seafloor, and $\Delta T_{\text{NMO,direct}}$ is given by equation 31. This equation implies that the NMO stretch can be increased by the decrease of the water depth and the increase of offset. The derivation of equation 34 is given in Appendix C.

On the other hand, stretching for reflected wave NMO correction for $\tau \ll T_z$ is quantified by

$$\frac{\Delta\tau_{\text{NMO,reflected}}}{\tau} \approx \frac{\Delta T_{\text{NMO,reflected}}}{T_z}, \tag{35}$$

where T_z is two-way traveltime for the vertical propagation distance from source to the reflector, and $\Delta T_{\text{NMO,reflected}}$ is given by equation 32. This expression is the same as NMO stretch for two-way traveltime reflections for any surface source and surface receiver (Yilmaz, 2001).

Temporal resolution

We now analyze a combined effect of the two DAS arrays associated with pulse width L_W and gauge length L_G on the temporal resolution of a plane wave propagating with velocity v and the grazing angle θ to the fiber axis. The effective fiber length of the combined array is the summation of the length of the two arrays, i.e., $L_{\text{effective}} = L_W + L_G$. Then, the arrival time of a plane wave at the two ends of this effective array is different by $\Delta\tau_{\text{DAS}} = (L_{\text{effective}} \cos\theta)/v$. A plane wave with a dominant period τ is transformed by DAS arrays to be extended along the time axis by this time delay. Hence, the ratio of the time delay to the dominant period of the wave is determined by

$$\frac{\Delta\tau_{\text{DAS}}}{\tau} = \frac{f\,(L_G + L_W)}{v}\cos\theta, \tag{36}$$

where $f = 1/\tau$ is the dominant frequency of the wave, and $\cos\theta = h_x/\sqrt{z^2 + h_x^2 + h_y^2}$. The ratio of the time delay to the wave period given by this equation may be interpreted as the stretching due to DAS response, since it is similar to the definition of NMO stretching. DAS stretching vanishes at the zero inline offset, where the wave propagates in the perpendicular direction to the fiber axis. Therefore, DAS stretching can be neglected for the data at nearly zero inline offset, while NMO stretching dominates the temporal resolution of the final images.

Image quality

The quality of an image can be evaluated by its signal-to-noise ratio (S/N). Hence, we use the S/N to quantitatively compare the quality of the DAS and streamer images. In our analysis, S/N of the i^{th} trace is defined as the ratio of the power of the signal ($P_{\text{signal},i}$)

within the trace to the average background noise power (P_{noise}) of the whole survey:

$$(\text{S/N})_i = \frac{P_{\text{signal},i}}{P_{\text{noise}}} = \left(\frac{A_{\text{signal},i}}{A_{\text{noise}}}\right)^2, \tag{37}$$

where $A_{\text{signal},i}$ is the RMS amplitude of the samples within the signal window from the i^{th} trace, and A_{noise} is the RMS amplitude of the samples within the background noise window from all of the traces. The ratio can be expressed in decibels (dB) as

$$(\text{S/N})_{\text{dB}} = 10 \log_{10} (\text{S/N}) . \tag{38}$$

RESULTS AND DISCUSSION

The key seismic imaging from DAS data begins with NMO corrections. Figure 16 illustrates the results of NMO corrections for direct wave and reflected waves in a super shot gather of the real data. The figure illustrates a supergather at shot number 2161, which is approximately at 2877 m distance on the cable, which is aligned with the horizontal axis in Figure 17. An offset trace in a supergather is derived by summing the seismic traces from nearby shots at the same offset bin. Supergathering can significantly enhance the S/N. However, it typically causes lower temporal resolution, as it stacks the waves with inconsistent phases. This supergathering technique is also applied to enhance the key seismic events for velocity analysis. The NMO corrections for direct wave and reflected waves are carried out independently after noise attenuation, redatuming to sea surface, and data regularization. The velocity models used in the NMO corrections are obtained by time-velocity scanning semblance analysis, where the velocity in water is assumed to be 1490 m/s. Note that the minimum offset in this shot gather is about 30 m. Hence, the first arrivals in all of the existing traces in this gather are reflected waves, not the direct wave.

After NMO corrections are applied, we mute the data with severe NMO stretch at far

offset and stack all the traces below the mute function. Then, two stacked section are derived, i.e., one from direct wave and the other from reflected waves. After stacking the NMO corrected gathers of DAS data, we combine the two stacked sections by summing the traces from the same shot. Then, we broaden the amplitude spectrum to be comparable with the reference seismic data from the streamer. We finally apply zero-offset time migration to the stacked data and compare the result with the image from streamer data in Figure 17. Figures 17a and 17b show the migrated images from streamer and DAS, respectively. The DAS image contains stronger high-frequency noise than the streamer image. The dominant frequency of DAS image is also somewhat lower, and the bandwidth is narrower than the streamer image.

We observe that the DAS image below the seafloor is contaminated by high-frequency noise, while the streamer image is somewhat cleaner. Therefore, we apply additional signal enhancement processing to the image by trace mixing of surrounding 21 traces and applying a high-cut filter at 480 Hz. These additional steps are applied to both streamer and DAS images, and the results are shown in Figures 17c and 17d, respectively. After signal enhancement, the continuity of the seafloor images is improved, and the subsurface reflections in the images become obvious and easy to interpret. Key seismic reflections can be observed in both images as highlighted by the yellow arrows in the figures. However, the signal enhancement reduces the frequency bandwidth and, hence, the image resolution. Therefore, the trade-off between enhancing the signal and maintaining the frequency bandwidth should carefully be tested to optimize the DAS image quality.

The geological image from streamer data results from seismic reflections, while the direct wave does not penetrate through any structure below the seafloor. On the other hand, the DAS seismic imaging uses both direct wave and reflections to construct the geological image.

Figure 17d illustrates that the seafloor and underlying subsurface structures can be imaged from DAS seismic data by our processing sequence. The seafloor and subsurface image from DAS data is comparable with the reference image from streamer data in Figure 17c. Note that the DAS image represents the image at a different position from the streamer data, since their receiver positions are different. Therefore, the subsurface structures in the images from streamer and DAS are slightly different.

We observe that the DAS image has low resolution in the shallowest part of the line between 2500 m and 2700 m, where the crossline offset is larger than the water depth. The primary reason is that our DAS data lack near-offset information, while the water depth is shallow at these locations. Therefore, the effect of NMO stretch becomes significant and causes a low dominant frequency content in the NMO result, especially for the water bottom event. Note that NMO stretch for the water bottom event depends on water depth and offset according to equation 34. The stretch increases with the decrease of the water depth and the increase of offset. Figure 18a illustrates the variations of water depth and minimum offset at different receiver positions. The minimum offset is the crossline offset (h_y) as illustrated in Figure 6. The source-to-cable distance (d) is also plotted in Figure 18a. In addition, Figure 18b shows the minimum stretch associated with the water bottom event. The minimum offset for the towed streamer is assumed to be 10 m throughout the survey. We observe that the minimum NMO stretch for DAS data is significantly larger than the minimum stretch for towed streamer data. Thus, the water bottom image from DAS has lower resolution than the image from the towed streamer as shown in Figure 17. The resolution of the DAS image is extremely low in the shallow water area at 2500–2600 m along the cable. To obtain a higher resolution image, we should have controlled the seismic source to be laterally closer to the DAS cable. That is, we must reduce the crossline offset

between source and the DAS cable during the survey, so that the NMO stretch is minimized. Then, a higher resolution seismic image can be achieved. The requirement of short crossline offset is crucial especially for any shallow water environment.

The effect of NMO stretch is illustrated in Figure 19, which compares a near trace gather of the DAS data before and after NMO correction for the direct wave. Each trace of the near trace gather is formed by stacking those seismic traces with inline offset less than 2 m from the corresponding shot gather. The gather represents the DAS data with nearly zero inline offset. That is, the offset of each trace in the gather is approximately equal to the crossline offset. In Figure 19a, we observe coherent seismic events (direct wave) before NMO correction that would contribute to the seafloor image. These events have comparable temporal resolution to the streamer data as shown in Figure 4. The key coherent seismic events are indicated by the black arrows in Figure 19. When the NMO correction for the direct wave is applied, the events are shifted in time and their characteristics are deformed by NMO stretch. NMO stretch deforms the wavelet to have lower frequency than the original form. As shown in Figure 19b, the stretch is enormous especially in the shallow water depth and large crossline offset like event "A". In contrast, we see less NMO stretch where the crossline offset is short, and the water is deep like event "B". This observation is aligned with the plot of minimum stretch in Figure 18b.

Figure 20a compares S/N in dB of the images from DAS and towed streamer around the water bottom. As plotted in Figure 17, the signal window is defined between the orange and green horizons, whereas the noise window is defined between the blue and orange horizons. We observe that the images from the towed streamer data generally have higher S/N than the DAS images, especially when the seafloor is shallow. On the other hand, Figure 20b compares the normalized power spectrum of the images in the signal window from streamer

and DAS after the same postmigration signal enhancement processing. We observe that the DAS image has lower dominant frequency than the streamer image. Moreover, the DAS image has more low frequency content than the streamer image.

Limitations of the study

We emphasize that our comparison is not one-to-one in the sense that the streamer data result from the summation of the 24 hydrophone elements (approximately 7 m) into one single channel. Stacking of 24 hydrophone elements corresponds to an improved S/N of the square root of the number of stacking elements (nearly 5 times in this case). This is the major explanation why the raw streamer data have less noise compared to the raw DAS data. The DAS data are recorded from each sensing element with a gauge length of 4 m. Furthermore, under an angle mute function, we sum the recorded data from at least 40 channels of 2 m spacing (approximately 80 m) with obvious signals as observed in Figure 5 to form a single trace of the DAS image in Figures 17b and 17d. The multi-channel summation of the DAS data significantly enhances the S/N. However, the optimal number of channels to be summed is still limited by the desired temporal resolution associated with the offset-dependent NMO stretch. Therefore, we recommend testing the mute function for stacking in order to find a compromise between the signal enhancement and the temporal resolution.

Our seismic analysis covers the range from 160–480 Hz, corresponding to the wavelengths in the range of 9.4 to 3.1 m with the velocity of 1490 m/s. However, the bandwidth of the seismic source used in this experiment ranges from 350–1000 Hz with the dominant frequency at about 600 Hz. For wave velocities in the order of 1490 m/s, this corresponds

to wavelengths in the range of 4.3 to 1.5 m, with the dominant energy at a wavelength of 2.5 m. Thus, with a DAS interrogator operating with a 4 m gauge length, the seismic waves propagating in parallel to the cable with frequency greater than the 375 Hz notch cannot be properly resolved by DAS (see Figures 9 and 10 for DAS array response). Using a seismic source with stronger low frequency emission or operating the DAS interrogator at shorter gauge lengths should, therefore, improve the DAS image resolution. Furthermore, with a more powerful source at low frequencies, it might be possible to utilize more DAS channels at larger inline offsets (a longer cable length) to construct a larger aperture which might improve the spatial resolution and provide deeper imaging capabilities with DAS. Note that the seismic source used in our experiment is relatively weak compared to conventional seismic sources such as air guns.

Our major objective of this article is to achieve a qualitative comparison of the two types of data to demonstrate the enormous potential for DAS data, despite its higher background noise level. The tremendous advantage for the DAS data is the number of channels in the long fiber optic cable. We aim to indicate that it is possible for DAS to record data over a long distance (several kilometers) to form subsurface images with comparable quality to those formed with the conventional streamer. The advantage of having excessive receivers over a long distance can be exploited for several other applications, such as tracking the positions of marine vessels, marine mammals, earthquakes and so on. However, this article is limited to a simple comparison of conventional seismic imaging to DAS imaging for seismic exploration based on different acquisition geometries.

The results shown in this article clearly prove that we can use DAS cables together with controlled seismic sources to construct a subsurface image comparable to a conventional seismic survey using towed streamers. To obtain a DAS image with high quality and high

S/N, we require sufficient source energy within the frequency range limited by the gauge length, which implies the spatial resolution of DAS. Moreover, we have to minimize the crossline offset between the source and the DAS cable during the survey to prevent excessive stretch and improve the image resolution. Thus, we can conclude that it is possible to use DAS from existing dark fiber optic cables together with appropriate seismic sources for subsurface imaging. If a conventional seismic survey is conducted above recording DAS cables, the near-surface seismic image from DAS can be obtained and used for geohazard analysis prior to any construction on the seafloor. Hence, we envisage many possibilities of DAS to support various subsurface exploration activities.

CONCLUSION

We can produce subsurface images from seismic data acquired by DAS in a submarine telecommunication cable. The quality of the images can be improved by using a seismic source with sufficiently large energy within the low-frequency range matching the spatial resolution of DAS. A low frequency seismic source would also improve the penetration to deeper geological structures, and, hence, deeper seismic images. The temporal resolution can be improved by minimizing the crossline offset between seismic sources and the DAS cable. For water depths larger than the offset range used for DAS imaging, we find that DAS and hydrophone data have about the same quality. The DAS recording can be carried out simultaneously with any conventional seismic survey to support geohazard analysis below the seafloor and various subsurface exploration activities. The operational advantages of DAS over node systems and the validity of DAS for near-surface seismic imaging will sustain the growth of DAS in the seabed seismic market.

ACKNOWLEDGMENTS

The authors acknowledge the Norwegian Research Council, and the sponsors of GAMES (Geophysics and Applied Mathematics in Exploration and Safe production Project; Grant no. 294404), Digimon ACT Project (Grant no. 299622), and Centre for Geophysical Forecasting (CGF; Grant no. 309960) at NTNU for financial support. The authors also thank the crew onboard R/V Gunnerus for assistance during the field work, Alcatel Submarine Networks for lending an OptoDAS interrogator, Shearwater GeoServices Software for Reveal software used in our analysis, Trond Larsen and KystTele for the access to the optical fiber, and Eirik Larsen for assistance in facilitating the DAS experiment.

APPENDIX A

DISTANCE BETWEEN SOURCE AND CABLE

From Figure 6, we define that t_0 is the UTC time when the source is fired, t is the UTC time when the direct wave arrives at a receiver, and τ is its traveltime from the source to the receiver. Thus,

$$\tau = t - t_0. \tag{A-1}$$

Assuming the constant velocity v, we can compute the travel distance of the direct wave from source to the receiver with the inline offset h_x as follows:

$$v\tau = \sqrt{d^2 + h_x^2}, \tag{A-2}$$

where d is the distance between source and the DAS cable. Hence, the traveltime of the direct wave can be written as a function of the inline offset h_x as follows:

$$\tau_{\{h_x\}} = \frac{1}{v}\sqrt{d^2 + h_x^2}. \tag{A-3}$$

The subscript on variable τ denotes its functional dependence on the inline offset h_x. To the receiver at zero inline offset ($h_x = 0$), the traveltime has a minimum at

$$\tau_{\{h_x=0\}} = \frac{d}{v}. \tag{A-4}$$

Hence, the difference between the traveltime at zero inline offset and the traveltime at an arbitrary offset is defined as follows:

$$\Delta\tau = \tau_{\{h_x\}} - \tau_{\{h_x=0\}} = \frac{1}{v}\sqrt{d^2 + h_x^2} - \frac{d}{v}. \tag{A-5}$$

Rearranging equation A-5, we obtain equation 24 via the following steps:

$$\Delta\tau + \frac{d}{v} = \frac{1}{v}\sqrt{d^2 + h_x^2} \tag{A-6}$$

$$\left(\Delta\tau + \frac{d}{v}\right)^2 = \frac{1}{v^2}\left(d^2 + h_x^2\right) \tag{A-7}$$

$$(\Delta\tau)^2 + 2(\Delta\tau)\left(\frac{d}{v}\right) + \frac{d^2}{v^2} = \frac{d^2}{v^2} + \frac{h_x^2}{v^2} \tag{A-8}$$

$$d = \frac{v}{2\Delta\tau}\left(\frac{h_x^2}{v^2} - (\Delta\tau)^2\right). \tag{A-9}$$

APPENDIX B

DAS DATA PROCESSING SEQUENCE

The processing sequence for DAS data is listed below:

1. Do radial trace mixing by summing the seismic traces from neighboring shots (3:1 shots).
2. Apply a band-pass frequency filter for 160 Hz/ 20 dB – 960 Hz/ 20 dB.
3. Apply static correction to redatum both source and receivers to the sea surface.
4. Regularize data using offset bin spacing of 1 m.

5. Apply NMO correction to correct the traveltime from arbitrary offsets to zero offset for the two events below separately using different correction methods:
   (a) The direct arrival from source to the DAS receivers on the seafloor.
   (b) The primary reflections from the geological structures underlying the seafloor.
6. Attenuate multiple reflections in the Radon domain.
7. Mute the undesired NMO stretch at far offsets (0–30 degrees with 76 m preserved minimum offset)
8. Stack the NMO data from all offset bins.
9. Combine the NMO stacks from both the direct arrival and reflections to construct a zero-offset seismic reflection data set where source and receivers are virtually at the sea surface.
10. Apply spectral whitening.
11. Apply zero-offset time migration using the NMO velocity for primary reflections.
12. Do radial trace mixing by summing the seismic traces from surrounding 21 traces.
13. Apply a high-cut filter at 480 Hz/ 20 dB.

APPENDIX C

MOVEOUT STRETCH FOR DIRECT WAVE

Considering the DAS data after redatuming the source and receivers to the sea surface, the direct wave moveout equation associated with the onset of the wavelet with the arrival

time T_{direct} at offset h is given by equation 31. This expression can be rearranged as follows:

$$\left(T_{\text{direct}} - \frac{T_z}{2}\right)^2 = \frac{T_z^2}{4} + \frac{h^2}{v^2} \tag{C-1}$$

$$T_{\text{direct}}^2 - T_{\text{direct}}T_z + \frac{T_z^2}{4} = \frac{T_z^2}{4} + \frac{h^2}{v^2} \tag{C-2}$$

$$T_{\text{direct}}^2 - T_{\text{direct}}T_z = \frac{h^2}{v^2}. \tag{C-3}$$

After applying NMO correction for the direct wave, the wavelet of dominant period τ is stretched, then its dominant period becomes $\tau_{\text{NMO}} = \tau + \Delta\tau_{\text{NMO,direct}}$ as previously defined in equation 33. Thus, the moveout equation associated with the termination of this wavelet can be derived by replacing T_{direct} with $T_{\text{direct}} + \tau$, and replacing T_z with $T_z + \tau_{\text{NMO}}$ in equation C-3. That is,

$$\left(T_{\text{direct}} + \tau\right)^2 - \left(T_{\text{direct}} + \tau\right)\left(T_z + \tau + \Delta\tau_{\text{NMO,direct}}\right) = \frac{h^2}{v^2} \tag{C-4}$$

$$\begin{aligned} &\left(T_{\text{direct}}^2 + 2T_{\text{direct}}\tau + \tau^2\right) \\ &-T_{\text{direct}}T_z - T_{\text{direct}}\tau - T_{\text{direct}}\Delta\tau_{\text{NMO,direct}} \\ &-\tau T_z - \tau^2 - \tau\Delta\tau_{\text{NMO,direct}} = \frac{h^2}{v^2} \end{aligned} \tag{C-5}$$

$$\begin{aligned} &\left[\left(T_{\text{direct}}^2 - T_{\text{direct}}T_z\right) - \frac{h^2}{v^2}\right] \\ &+ \left(T_{\text{direct}} - T_z\right)\tau = \left(T_{\text{direct}} + \tau\right)\Delta\tau_{\text{NMO,direct}}. \end{aligned} \tag{C-6}$$

The first term on the left-hand side of equation C-6 becomes zero by the relation in equation C-3. Accordingly, using the definition of $\Delta T_{\text{NMO,direct}}$ from equation 30, we can derive the moveout stretch for direct wave from equation C-6 as follows:

$$\left(\Delta T_{\text{NMO,direct}}\right)\tau = \left(T_z + \Delta T_{\text{NMO,direct}} + \tau\right)\Delta\tau_{\text{NMO,direct}} \tag{C-7}$$

$$\frac{\Delta\tau_{\text{NMO,direct}}}{\tau} = \frac{\Delta T_{\text{NMO,direct}}}{T_z + \Delta T_{\text{NMO,direct}} + \tau}. \tag{C-8}$$

Assuming that $\tau \ll T_z$, the moveout stretch for direct wave can be approximated by the following expression:

$$\frac{\Delta\tau_{\mathrm{NMO,direct}}}{\tau} \approx \frac{\Delta T_{\mathrm{NMO,direct}}}{T_z + \Delta T_{\mathrm{NMO,direct}}}. \tag{C-9}$$

REFERENCES

Ajo-Franklin, J., S. Dou, T. Daley, B. Freifeld, M. Robertson, C. Ulrich, T. Wood, I. Eckblaw, N. Lindsey, E. Martin, and A. Wagner, 2017, Time-lapse surface wave monitoring of permafrost thaw using distributed acoustic sensing and a permanent automated seismic source: SEG Technical Program Expanded Abstracts 2017, SEG, 5223–5227.

Ajo-Franklin, J., N. Lindsey, T. Daley, B. Freifeld, M. Robertson, C. Ulrich, S. Dou, E. Martin, and A. Wagner, 2015, A field test of distributed acoustic sensing for ambient noise recording: SEG Technical Program Expanded Abstracts 2015, SEG, 2620–2624.

Ajo-Franklin, J. B., S. Dou, N. J. Lindsey, I. Monga, C. Tracy, M. Robertson, V. Rodriguez Tribaldos, C. Ulrich, B. Freifeld, T. Daley, and X. Li, 2019, Distributed acoustic sensing using dark fiber for near-surface characterization and broadband seismic event detection: Scientific Reports, **9**, 1328.

Bakku, S. K., 2015, Fracture characterization from seismic measurements in a borehole: PhD thesis, Massachusetts Institute of Technology.

Bakulin, A., I. Silvestrov, and R. Pevzner, 2019, Surface seismic with DAS changes land acquisition: Presented at the SPE Middle East Oil and Gas Show and Conference, Society of Petroleum Engineers.

———, 2020, Surface seismics with DAS: An emerging alternative to modern point-sensor acquisition: The Leading Edge, **39**, 808–818.

Bertholds, A., and R. Dandliker, 1988, Determination of the individual strain-optic coefficients in single-mode optical fibres: Journal of Lightwave Technology, **6**, 17–20.

Biondi, B., E. Martin, S. Cole, M. Karrenbach, and N. Lindsey, 2017, Earthquakes analysis using data recorded by the Stanford DAS array: SEG Technical Program Expanded Abstracts 2017, SEG, 2752–2756.

Daley, T. M., B. M. Freifeld, J. Ajo-Franklin, S. Dou, R. Pevzner, V. Shulakova, S. Kashikar, D. E. Miller, J. Goetz, J. Henninges, and S. Lueth, 2013, Field testing of fiber-optic distributed acoustic sensing (DAS) for subsurface seismic monitoring: The Leading Edge, **32**, 699–706.

Dean, T., T. Brice, A. Hartog, E. Kragh, D. Molteni, and K. O'Connell, 2016, Distributed vibration sensing for seismic acquisition: The Leading Edge, **35**, 600–604.

Dean, T., T. Cuny, and A. H. Hartog, 2017, The effect of gauge length on axially incident P-waves measured using fibre optic distributed vibration sensing: Geophysical Prospecting, **65**, 184–193.

Dou, S., N. Lindsey, A. M. Wagner, T. M. Daley, B. Freifeld, M. Robertson, J. Peterson, C. Ulrich, E. R. Martin, and J. B. Ajo-Franklin, 2017, Distributed acoustic sensing for seismic monitoring of the near surface: A traffic-noise interferometry case study: Scientific Reports, **7**, 11620.

Drijkoningen, G. G., 2003, Lecture notes: Seismic data acquisition – TA3600: Delft University of Technology.

Fang, G., Y. E. Li, Y. Zhao, and E. R. Martin, 2020, Urban near-surface seismic monitoring using distributed acoustic sensing: Geophysical Research Letters, **47**, e2019GL086115.

Fernández-Ruiz, M. R., M. A. Soto, E. F. Williams, S. Martin-Lopez, Z. Zhan, M. Gonzalez-Herraez, and H. F. Martins, 2020, Distributed acoustic sensing for seismic activity monitoring: APL Photonics, **5**, 030901.

Hartog, A. H., 2017, An introduction to distributed optical fibre sensors, 1 ed.: CRC Press.

Kowarik, S., M.-T. Hussels, S. Chruscicki, S. Münzenberger, A. Lämmerhirt, P. Pohl, and M. Schubert, 2020, Fiber optic train monitoring with distributed acoustic sensing: Conventional and neural network data analysis: Sensors, **20**, 450.

Kuvshinov, B., 2016, Interaction of helically wound fibre-optic cables with plane seismic waves: Geophysical Prospecting, **64**, 671–688.

Landrø, M., and L. Amundsen, 2018, Introduction to exploration geophysics with recent advances: Bivrost.

Langhammer, J., M. Eriksrud, and H. Nakstad, 2010, Performance characteristics of 4C fiber optic ocean bottom cables for permanent reservoir monitoring: SEG Technical Program Expanded Abstracts 2010, SEG, 66–70.

L'Heureux, J.-S., L. Hansen, and O. Longva, 2009, Development of the submarine channel in front of the Nidelva River, Trondheimsfjorden, Norway: Marine Geology, **260**, 30–44.

Lindsey, N. J., T. C. Dawe, and J. B. Ajo-Franklin, 2019, Illuminating seafloor faults and ocean dynamics with dark fiber distributed acoustic sensing: Science, **366**, 1103–1107.

Lindsey, N. J., S. Yuan, A. Lellouch, L. Gualtieri, T. Lecocq, and B. Biondi, 2020, City-scale dark fiber DAS measurements of infrastructure use during the COVID-19 pandemic: Geophysical Research Letters, **47**, e2020GL089931.

Lumens, P. G. E., 2014, Fibre-optic sensing for application in oil and gas wells: PhD thesis, Technische Universiteit Eindhoven.

Martin, E. R., C. M. Castillo, S. Cole, P. S. Sawasdee, S. Yuan, R. Clapp, M. Karrenbach, and B. L. Biondi, 2017, Seismic monitoring leveraging existing telecom infrastructure at the SDASA: Active, passive, and ambient-noise analysis: The Leading Edge, **36**, 1025–1031.

Martin, E. R., F. Huot, Y. Ma, R. Cieplicki, S. Cole, M. Karrenbach, and B. L. Biondi, 2018, A seismic shift in scalable acquisition demands new processing: Fiber-optic seismic signal retrieval in urban areas with unsupervised learning for coherent noise removal: IEEE Signal Processing Magazine, **35**, 31–40.

Mateeva, A., J. Lopez, H. Potters, J. Mestayer, B. Cox, D. Kiyashchenko, P. Wills, S. Grandi, K. Hornman, B. Kuvshinov, W. Berlang, Z. Yang, and R. Detomo, 2014, Distributed acoustic sensing for reservoir monitoring with vertical seismic profiling: Geophysical Prospecting, **62**, 679–692.

Monrigal, O., I. de Jong, and H. Duarte, 2017, An ultra-high-resolution 3D marine seismic system for detailed site investigation: Near Surface Geophysics, **15**, 335–345.

Papp, B., D. Donno, J. E. Martin, and A. H. Hartog, 2017, A study of the geophysical response of distributed fibre optic acoustic sensors through laboratory-scale experiments: Geophysical response of fibre optic sensors: Geophysical Prospecting, **65**, 1186–1204.

Sladen, A., D. Rivet, J. P. Ampuero, L. De Barros, Y. Hello, G. Calbris, and P. Lamare, 2019, Distributed sensing of earthquakes and ocean-solid Earth interactions on seafloor telecom cables: Nature Communications, **10**, 5777.

Thomas, Y., B. Marsset, G. Westbrook, C. Grail, L. Géli, P. Henry, G. Çifçi, A. Rochat, and H. Saritas, 2012, Contribution of high-resolution 3D seismic near-seafloor imaging to reservoir-scale studies: application to the active North Anatolian Fault, Sea of Marmara: Near Surface Geophysics, **10**, 291–301.

Urosevic, M., A. Bona, S. Ziramov, R. Pevzner, K. Tertyshnikov, R. Martin, J. Dwyer, D. Felding, C. Guarin, and A. Foley, 2019, Seismic exploration of mineral resources in western australia with distribute acoustic sensing: 25th European Meeting of Environmental and Engineering Geophysics, EAGE, 1–5.

Vinje, V., J. E. Lie, V. Danielsen, P. E. Dhelle, R. Silliqi, C.-I. Nilsen, E. Hicks, and A. Camerer, 2017, Shooting over the seismic spread: First Break, **35**, 97–104.

Waagaard, O. H., E. Rønnekleiv, A. Haukanes, F. Stabo-Eeg, D. Thingbø, S. Forbord, S. E. Aasen, and J. K. Brenne, 2021, Real-time low noise distributed acoustic sensing in 171

km low loss fiber: OSA Continuum, **4**, 688–701.

Walter, F., D. Gräff, F. Lindner, P. Paitz, M. Köpfli, M. Chmiel, and A. Fichtner, 2020, Distributed acoustic sensing of microseismic sources and wave propagation in glaciated terrain: Nature Communications, **11**, 2436.

Wang, Y., H. Yuan, X. Liu, Q. Bai, H. Zhang, Y. Gao, and B. Jin, 2019, A comprehensive study of optical fiber acoustic sensing: IEEE Access, **7**, 85821–85837.

Williams, E. F., M. R. Fernández-Ruiz, R. Magalhaes, R. Vanthillo, Z. Zhan, M. González-Herráez, and H. F. Martins, 2019, Distributed sensing of microseisms and teleseisms with submarine dark fibers: Nature Communications, **10**, 5778.

Yilmaz, O., 2001, Seismic data analysis: SEG.

Yu, C., Z. Zhan, N. J. Lindsey, J. B. Ajo-Franklin, and M. Robertson, 2019, The potential of DAS in teleseismic studies: Insights from the Goldstone experiment: Geophysical Research Letters, **46**, 1320–1328.

Zhu, T., J. Shen, and E. R. Martin, 2021, Sensing earth and environment dynamics by telecommunication fiber-optic sensors: an urban experiment in Pennsylvania, USA: Solid Earth, **12**, 219–235.

LIST OF FIGURES

equation 15. The spherical divergence ($1/r$) is excluded in this plot. The source depth is 0.60 m below the sea surface, and the wave velocity is 1490 m/s.

8 The optical point strain variation with the grazing angle of a plane wave impinging the DAS cable with different coupling coefficients (α) (see equation 20).

9 The variation of the DAS array response ($L_G = L_W = 4.0852$ m) with the frequency and velocity of wave propagating in the same direction as the fiber axis ($\theta = 0$).

10 The variation of the DAS array response ($L_G = L_W = 4.0852$ m) with the frequency and grazing angle of wave in water, where $v = 1490$ m/s.

11 The total DAS receiver array response of the response to the strain field in Figure 8 and the DAS array response in Figure 10: (a) $\alpha = 0$, (b) $\alpha = 0.5$, and (c) $\alpha = 1$. Each plot is equivalent to the product of the point strain response with the associated coupling coefficient α in equation 20 and the DAS array response in equation 22.

12 Responses of DAS system in a straight fiber ($\alpha = 1$) to a spherical P wave from a point source at 0 m crossline offset: (a) the array response of source and its ghost with spherical divergence term applied, (b) the combined DAS array response to the strain field, and (c) the total response of both source and DAS arrays. The responses at key water depths are plotted at the bottom. Source is at 0.6 m depth and the wave propagates with 1490 m/s velocity at 600 Hz.

13 Responses of DAS system in a straight fiber ($\alpha = 1$) to a spherical P wave from a point source at 60 m crossline offset: (a) the array response of source and its ghost with spherical divergence term applied, (b) the combined DAS array response to the strain field, and (c) the total response of both source and DAS arrays. The responses at key water depths are plotted at the bottom. Source is at 0.6 m depth and the wave propagates with 1490 m/s velocity at 600 Hz.

14 A common receiver gather (channel number 1251 at 2555 m inline position) of DAS seismic records: (a) raw data, and (b) data after applying a band-pass filter of 160–960 Hz for illustration. The direct P wave from consecutive shots to the receiver on the seafloor is indicated by the yellow arrow. Polarity flips of the direct arrival are highlighted by the green arrows.

15 Description of NMO correction for the one-way traveltime of the direct wave in DAS recording system: (a) the geometry of the direct wave, and (b) the schematic plot of the direct wave in a shot gather before and after NMO correction. The NMO corrected traveltime of the direct wave is equal to the one-way traveltime along the vertical axis to the seafloor.

16 NMO corrections for the real DAS data set after redatuming to the sea surface and regularization. Supergathering the data from 21 shots around the shot number 2161, of which the position is approximately at 2877 m on the cable, is made to enhance S/N for illustration: (a) A super shot gather sorted by regularized absolute horizontal offsets from the source to the DAS receivers. (b) The result of NMO correction for direct wave. (c) The result of NMO correction for reflected wave. The dashed blue line is the direct wave event and the dashed orange line is a key reflection event, which are estimated by the associated time-velocity picks. The solid yellow line is the external mute function to be applied before stacking the data along offset.

17 Poststack time migrated seismic images from different data sets: (a) the reference image from a towed single-channel streamer with a 24-element hydrophone array of 7 m active length, (b) the image from seabed DAS with 4 m gauge length, (c) the image of (a) with additional signal enhancement applied, and (d) the image of (b) with the same enhancement applied. The seismic events associated with the water bottom and subsurface

reflections are presented in both images. Subsurface reflections in DAS image are highlighted by yellow arrows in comparison with the reference image. The horizontal axis is the distance along the cable. The horizons plotted in (c) and (d) define the signal and noise windows for computing the S/N and spectrum in Figure 20. Signal window is defined between orange and green horizons, whereas noise window is defined between blue and orange horizons.

18 Plots of the following variables at different positions along DAS cable: (a) the water depth (blue), the crossline horizontal offset from source to the DAS cable (orange), the distance between source and the DAS cable (green); and, (b) the minimum NMO stretch associated with the water bottom events in DAS data (solid blue line) and towed streamer data (dashed orange line).

19 Illustration of NMO stretch effect on a near trace gather of DAS data where sources and receivers are redatumed to the sea surface: (a) near trace gather from the DAS data with common inline offset, and (b) the same gather after NMO correction for the direct wave is applied. The black arrows indicate the two events before and after NMO correction as described in the texts.

20 QC plots corresponding to the seismic images from DAS (blue) and towed streamer (orange) with additional signal enhancement applied as shown in Figures 17c and 17d: (a) S/N at different seismic traces, and (b) normalized amplitude spectra within the signal and noise windows. Signal window is defined between orange and green horizons, whereas noise window is defined between the blue and orange horizons in Figure 17.

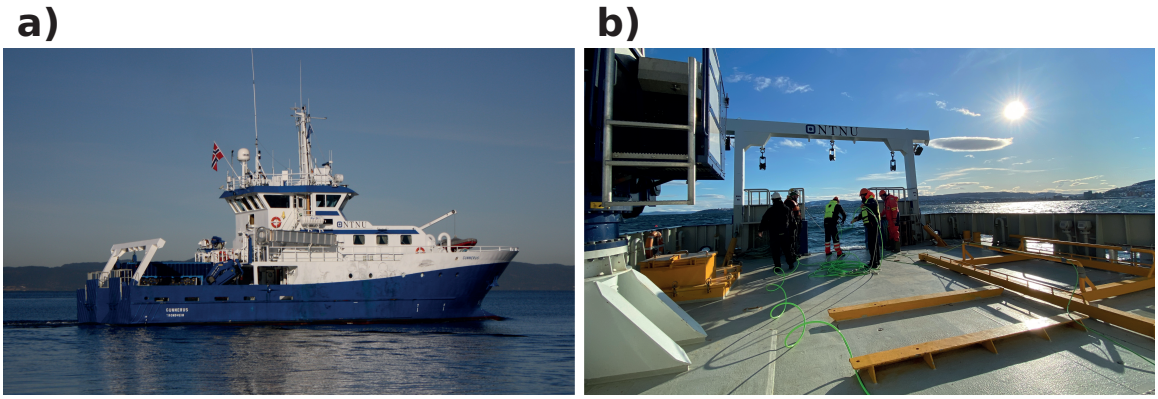

Figure 1: Photos of (a) NTNU's research vessel Gunnerus (retrieved from `https://www.flickr.com/photos/trondheimhavn/5036332012/`), and (b) the crew in action to recover the HMS-620 Bubble Gun source.

– **GEO-2020-0834.R2**

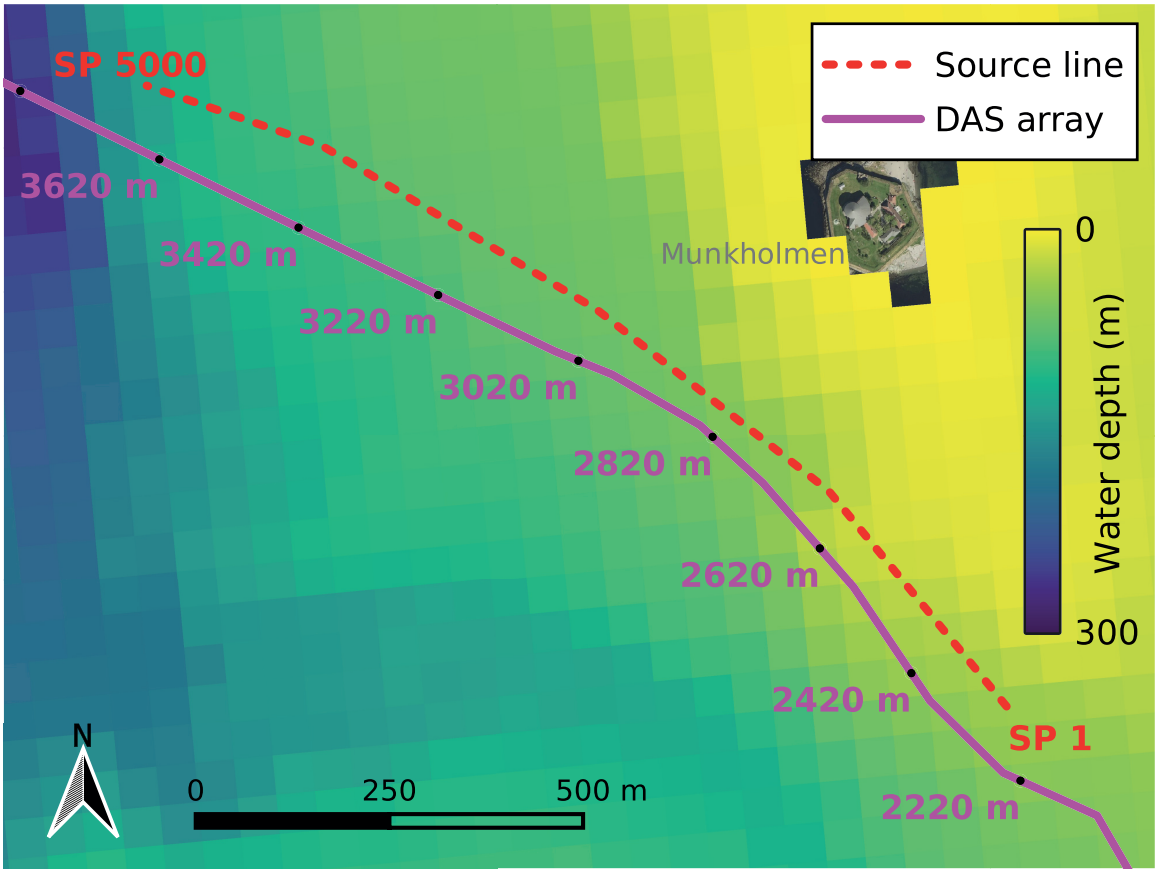

Figure 2: Source and receiver location map of the marine seismic survey in the Trondheimsfjord, Norway. The vessel route (dashed red line) is controlled to be close to the DAS receiver cable (solid magenta line) as much as possible. The receiver positions are annotated as the distance along the DAS cable. The background water depth map is shown by courtesy of Kartverket (Norwegian Mapping Authority).

– **GEO-2020-0834.R2**

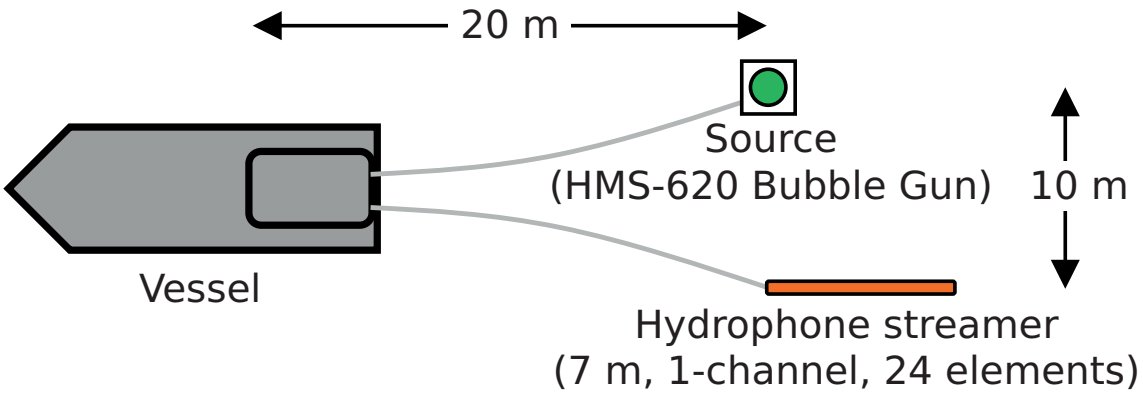

Figure 3: Top view of the acquisition layout. The source and the streamer are towed approximately 20 m behind R/V Gunnerus. The diagram is not to scale.

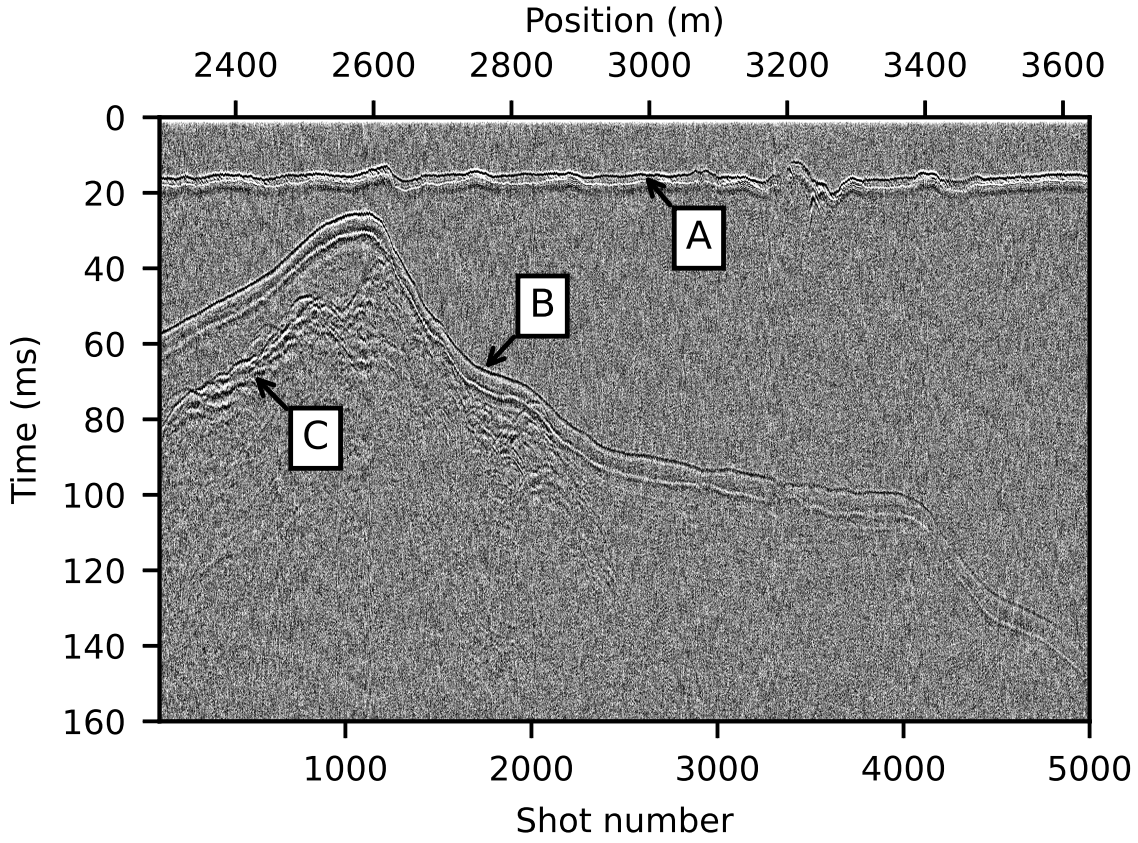

Figure 4: A common-channel seismic gather recorded by a towed single-channel streamer. It is also a common-offset gather at 10 m offset. The direct wave (A) and the reflections from the seafloor (B) and subsurface bedrock (C) are highlighted.

– **GEO-2020-0834.R2**

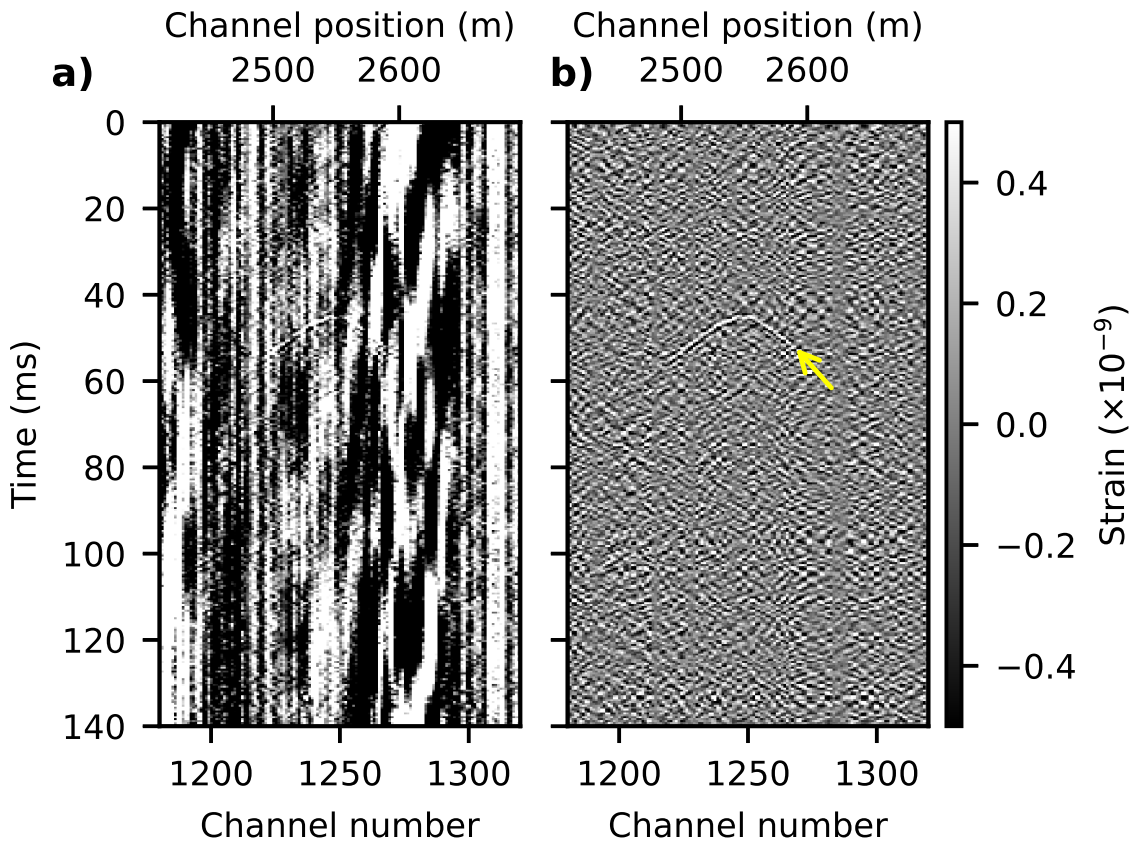

Figure 5: A shot profile (shot number 951 at 2546 m inline position) of multi-channel DAS seismic records: (a) raw data, and (b) data after applying a band-pass filter of 160–960 Hz for illustration. The yellow arrow indicates the direct wave from source to the seabed receivers.

– **GEO-2020-0834.R2**

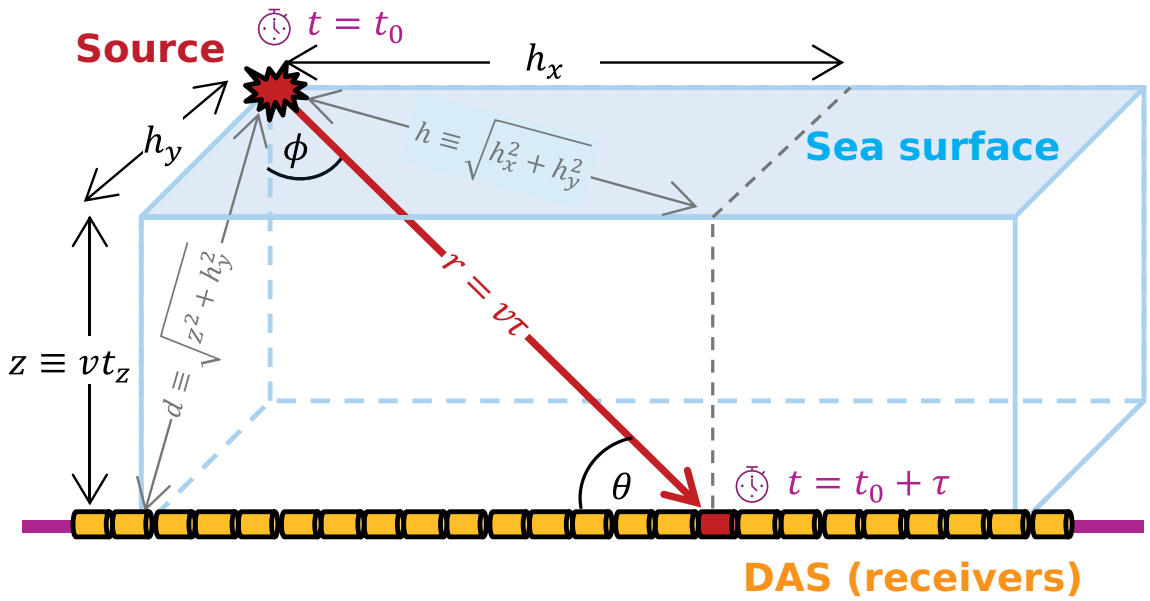

Figure 6: DAS recording system and its seismic source, where τ is the traveltime of direct wave propagation with velocity v from source to a receiver at the inline offset h_x. At the receiver with zero inline offset ($h_x = 0$), the traveltime is shortest and equal to $\tau_{\{h_x=0\}} = d/v$, where d is the distance between the source and DAS cable.

– **GEO-2020-0834.R2**

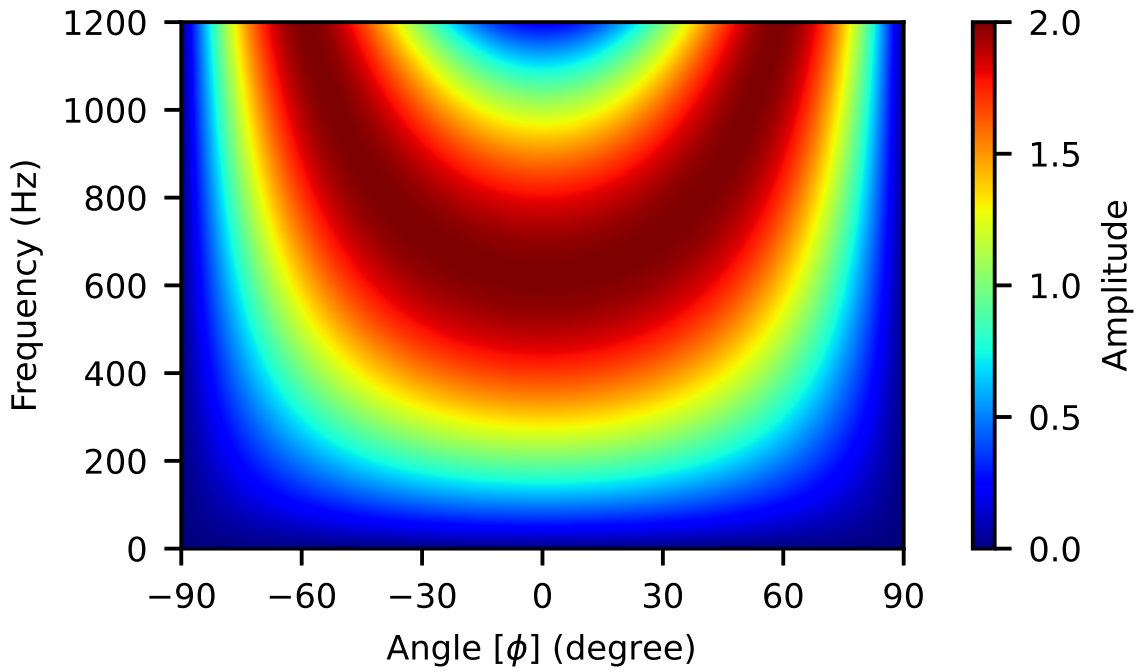

Figure 7: Amplitude directivity of a harmonic point source with ghost as a function of wave frequency and propagating angle from the vertical axis as defined in the square bracket in equation 15. The spherical divergence $(1/r)$ is excluded in this plot. The source depth is 0.60 m below the sea surface, and the wave velocity is 1490 m/s.

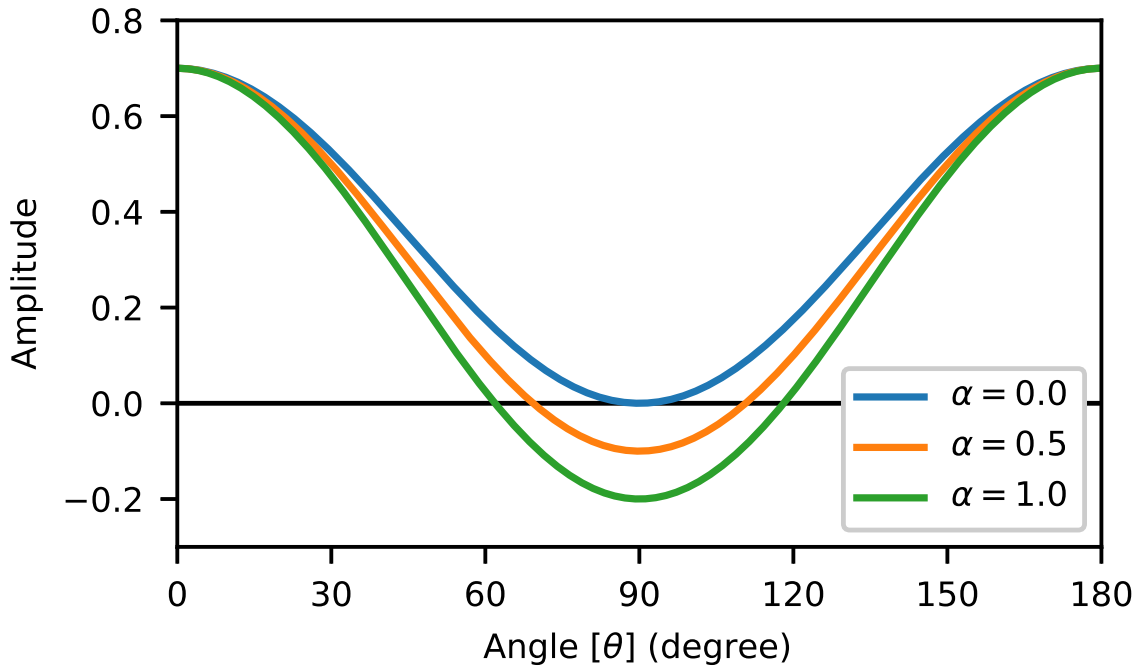

Figure 8: The optical point strain variation with the grazing angle of a plane wave impinging the DAS cable with different coupling coefficients (α) (see equation 20).

– **GEO-2020-0834.R2**

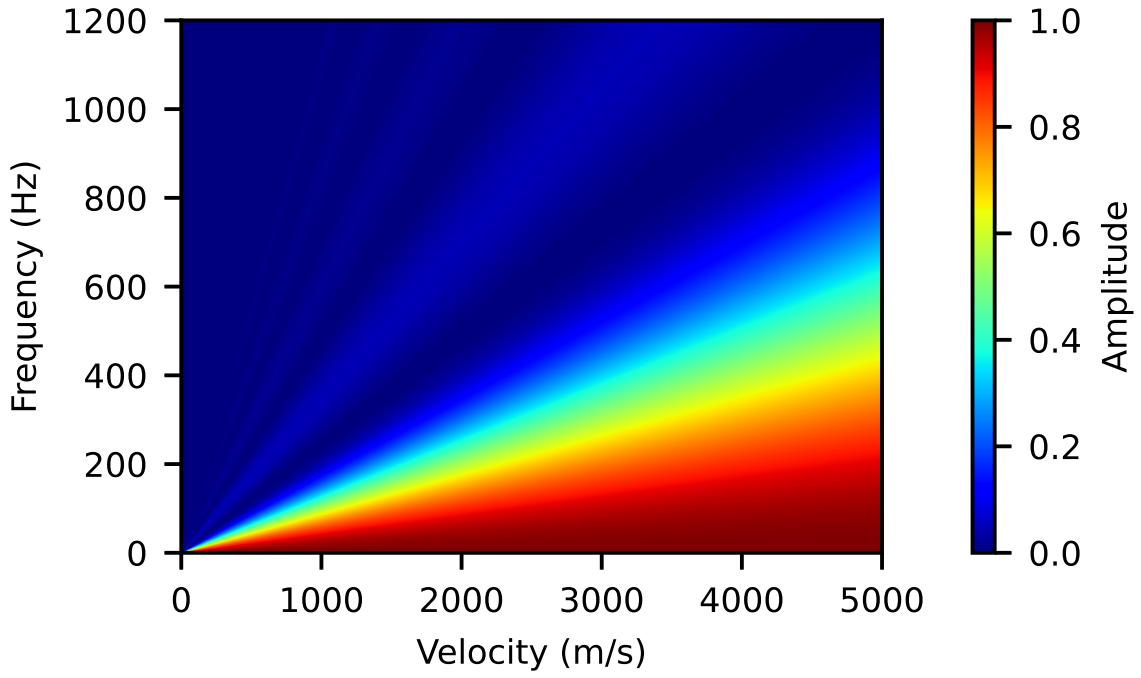

Figure 9: The variation of the DAS array response ($L_G = L_W = 4.0852$ m) with the frequency and velocity of wave propagating in the same direction as the fiber axis ($\theta = 0$).

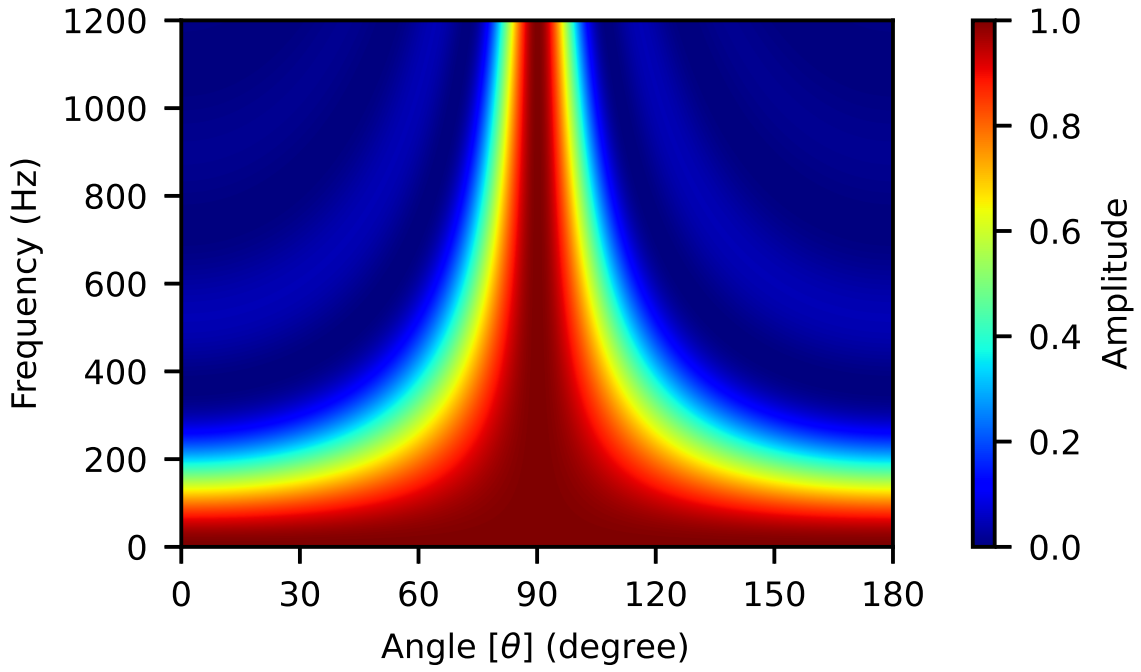

Figure 10: The variation of the DAS array response ($L_G = L_W = 4.0852$ m) with the frequency and grazing angle of wave in water, where $v = 1490$ m/s.

– **GEO-2020-0834.R2**

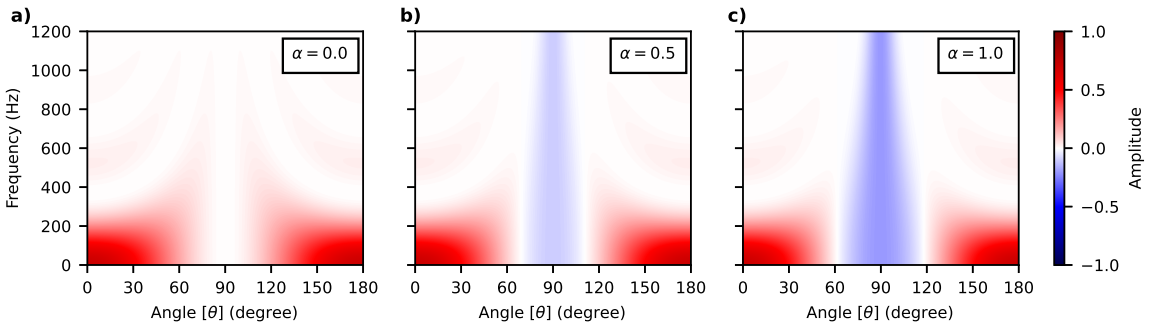

Figure 11: The total DAS receiver array response of the response to the strain field in Figure 8 and the DAS array response in Figure 10: (a) $\alpha = 0$, (b) $\alpha = 0.5$, and (c) $\alpha = 1$. Each plot is equivalent to the product of the point strain response with the associated coupling coefficient α in equation 20 and the DAS array response in equation 22.

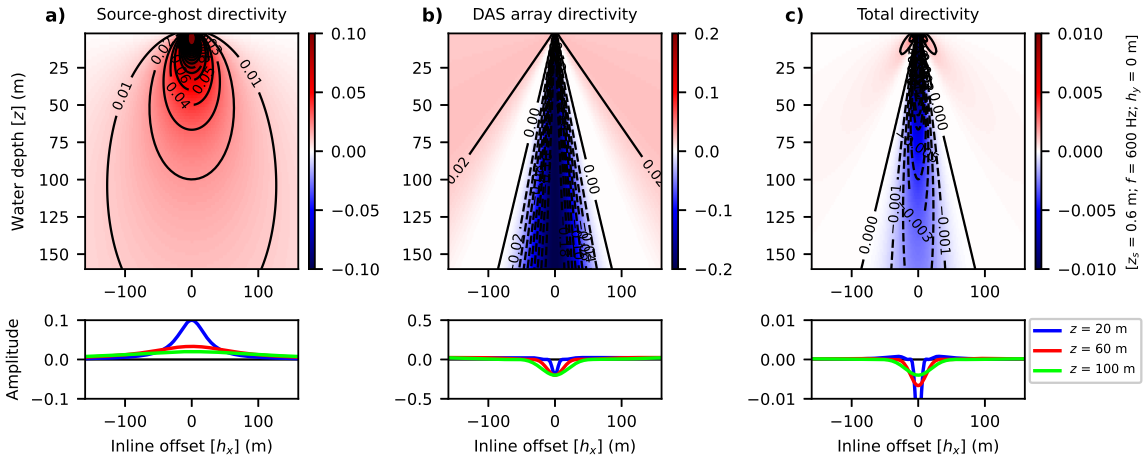

Figure 12: Responses of DAS system in a straight fiber ($\alpha = 1$) to a spherical P wave from a point source at 0 m crossline offset: (a) the array response of source and its ghost with spherical divergence term applied, (b) the combined DAS array response to the strain field, and (c) the total response of both source and DAS arrays. The responses at key water depths are plotted at the bottom. Source is at 0.6 m depth and the wave propagates with 1490 m/s velocity at 600 Hz.

– **GEO-2020-0834.R2**

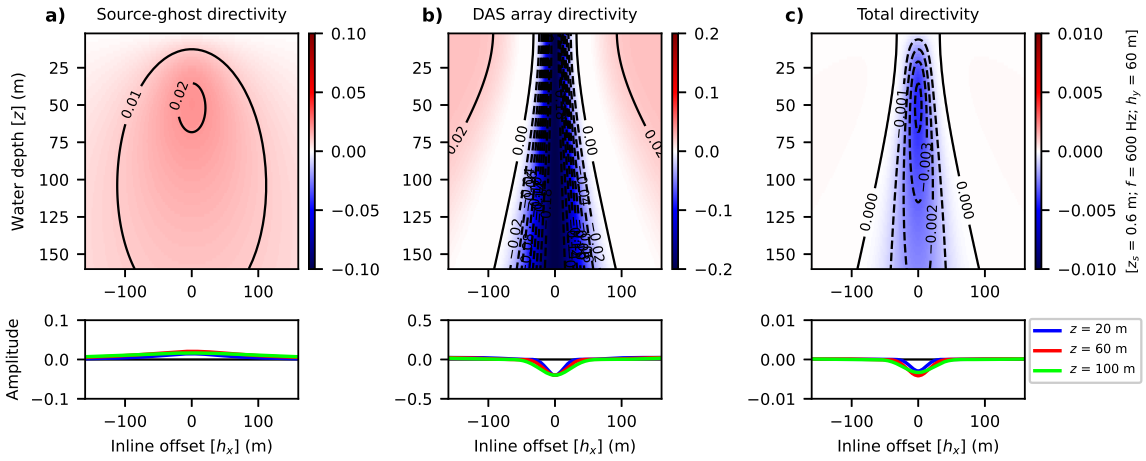

Figure 13: Responses of DAS system in a straight fiber ($\alpha = 1$) to a spherical P wave from a point source at 60 m crossline offset: (a) the array response of source and its ghost with spherical divergence term applied, (b) the combined DAS array response to the strain field, and (c) the total response of both source and DAS arrays. The responses at key water depths are plotted at the bottom. Source is at 0.6 m depth and the wave propagates with 1490 m/s velocity at 600 Hz.

– **GEO-2020-0834.R2**

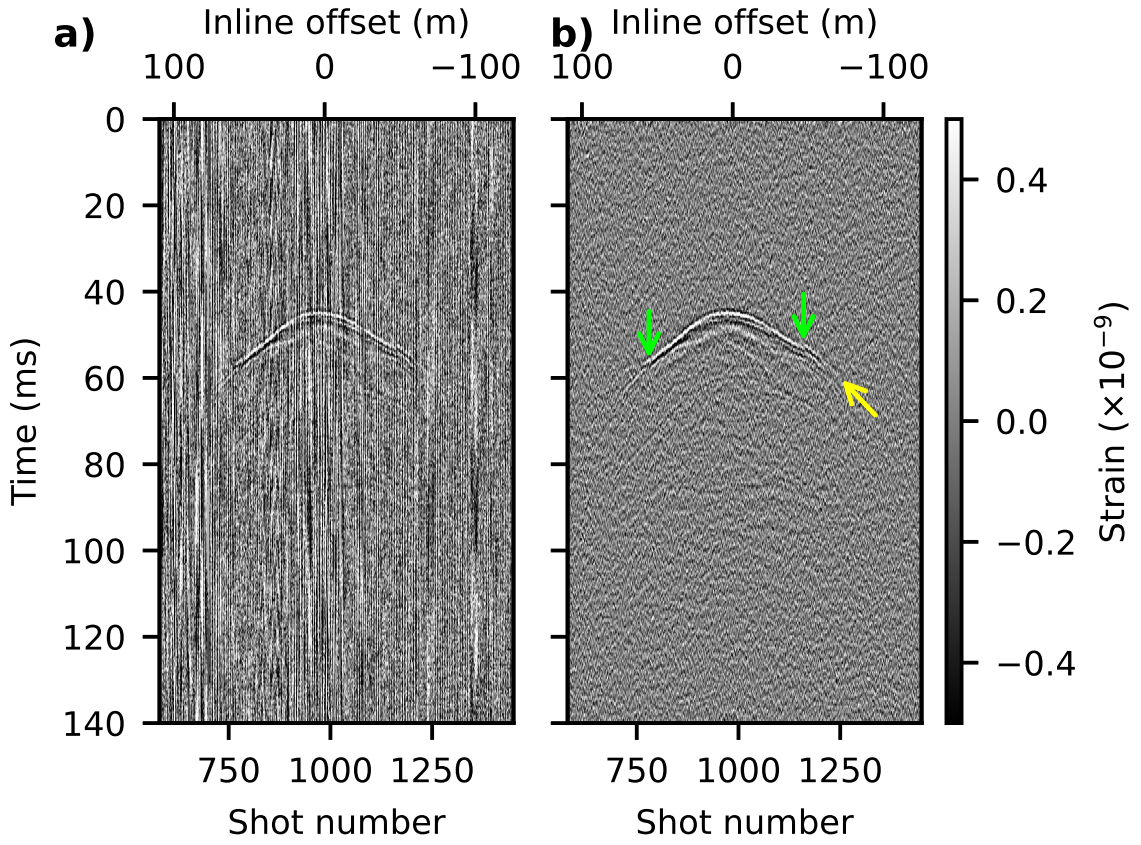

Figure 14: A common receiver gather (channel number 1251 at 2555 m inline position) of DAS seismic records: (a) raw data, and (b) data after applying a band-pass filter of 160–960 Hz for illustration. The direct P wave from consecutive shots to the receiver on the seafloor is indicated by the yellow arrow. Polarity flips of the direct arrival are highlighted by the green arrows.

– **GEO-2020-0834.R2**

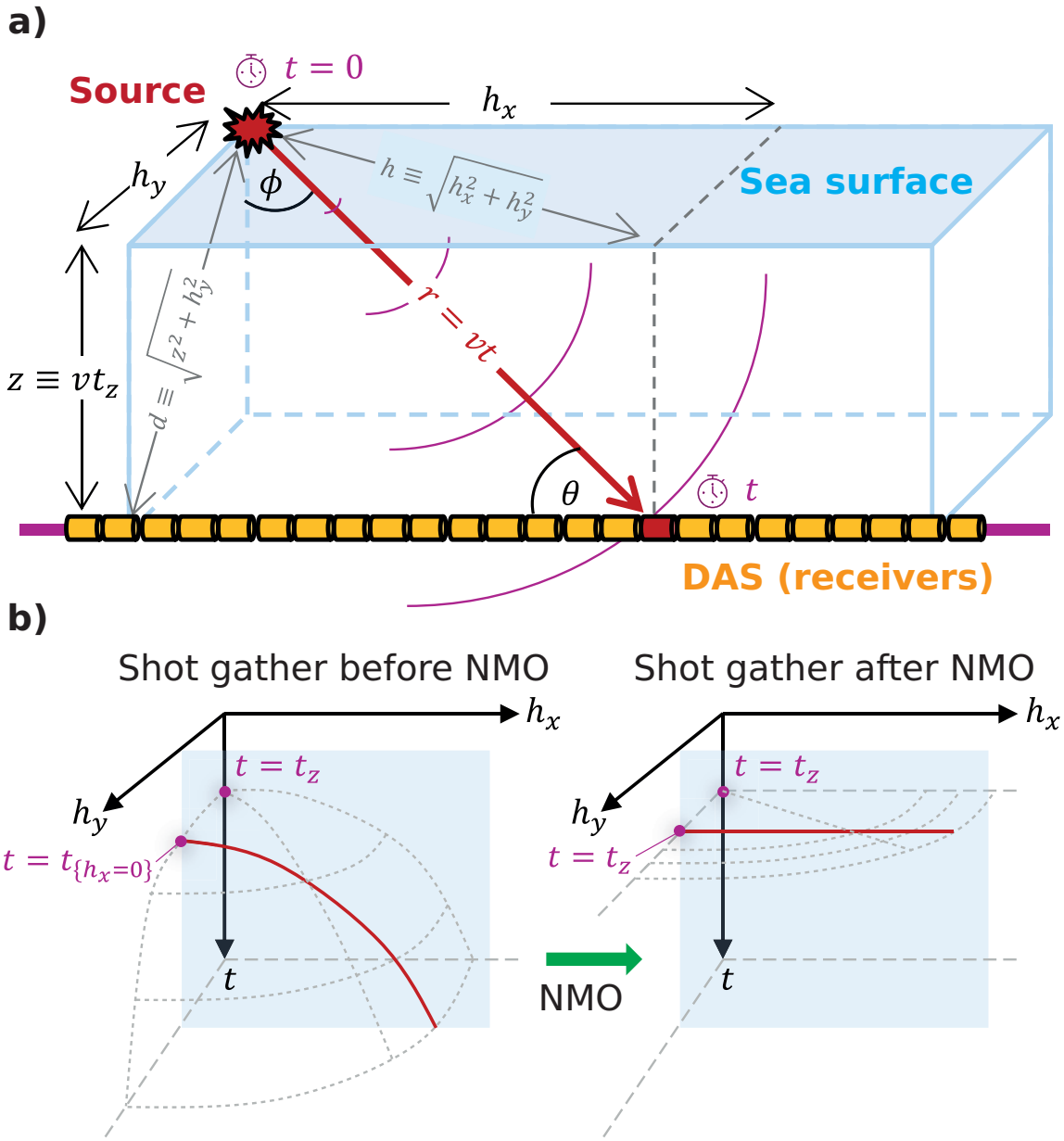

Figure 15: Description of NMO correction for the one-way traveltime of the direct wave in DAS recording system: (a) the geometry of the direct wave, and (b) the schematic plot of the direct wave in a shot gather before and after NMO correction. The NMO corrected traveltime of the direct wave is equal to the one-way traveltime along the vertical axis to the seafloor.

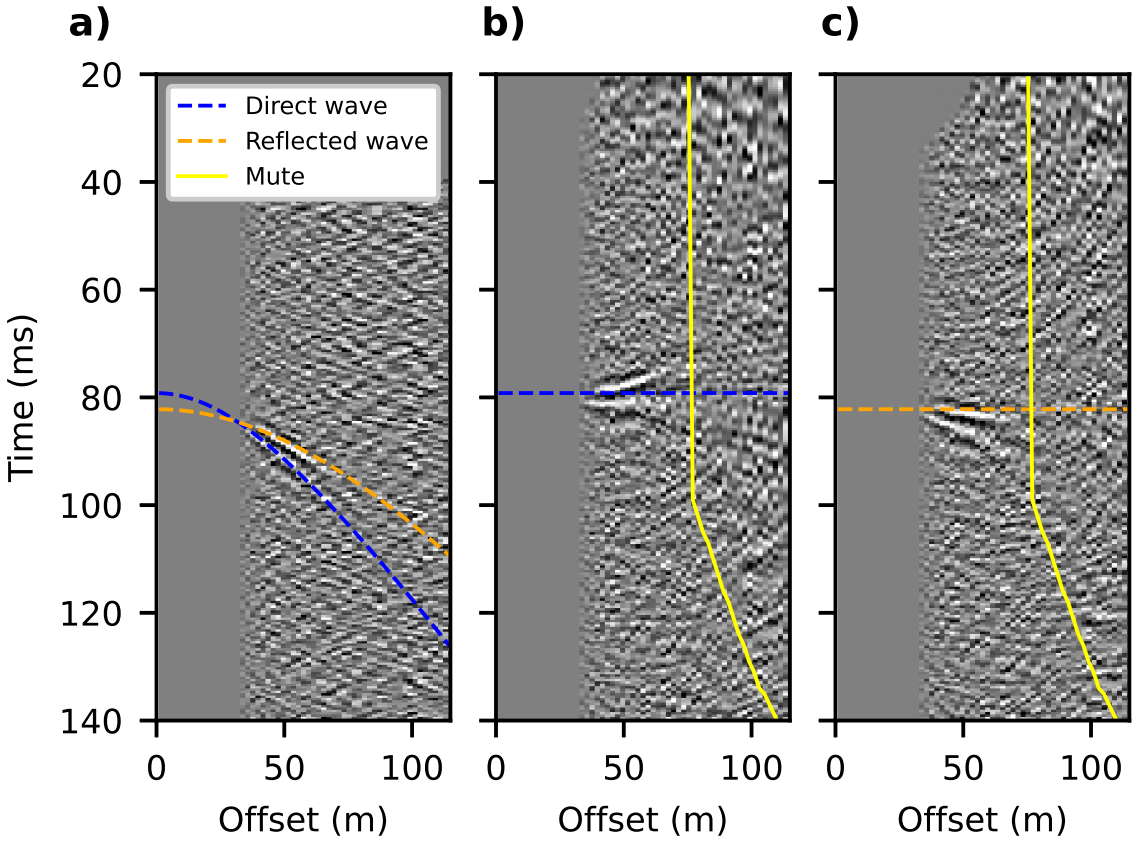

Figure 16: NMO corrections for the real DAS data set after redatuming to the sea surface and regularization. Supergathering the data from 21 shots around the shot number 2161, of which the position is approximately at 2877 m on the cable, is made to enhance S/N for illustration: (a) A super shot gather sorted by regularized absolute horizontal offsets from the source to the DAS receivers. (b) The result of NMO correction for direct wave. (c) The result of NMO correction for reflected wave. The dashed blue line is the direct wave event and the dashed orange line is a key reflection event, which are estimated by the associated time-velocity picks. The solid yellow line is the external mute function to be applied before stacking the data along offset.

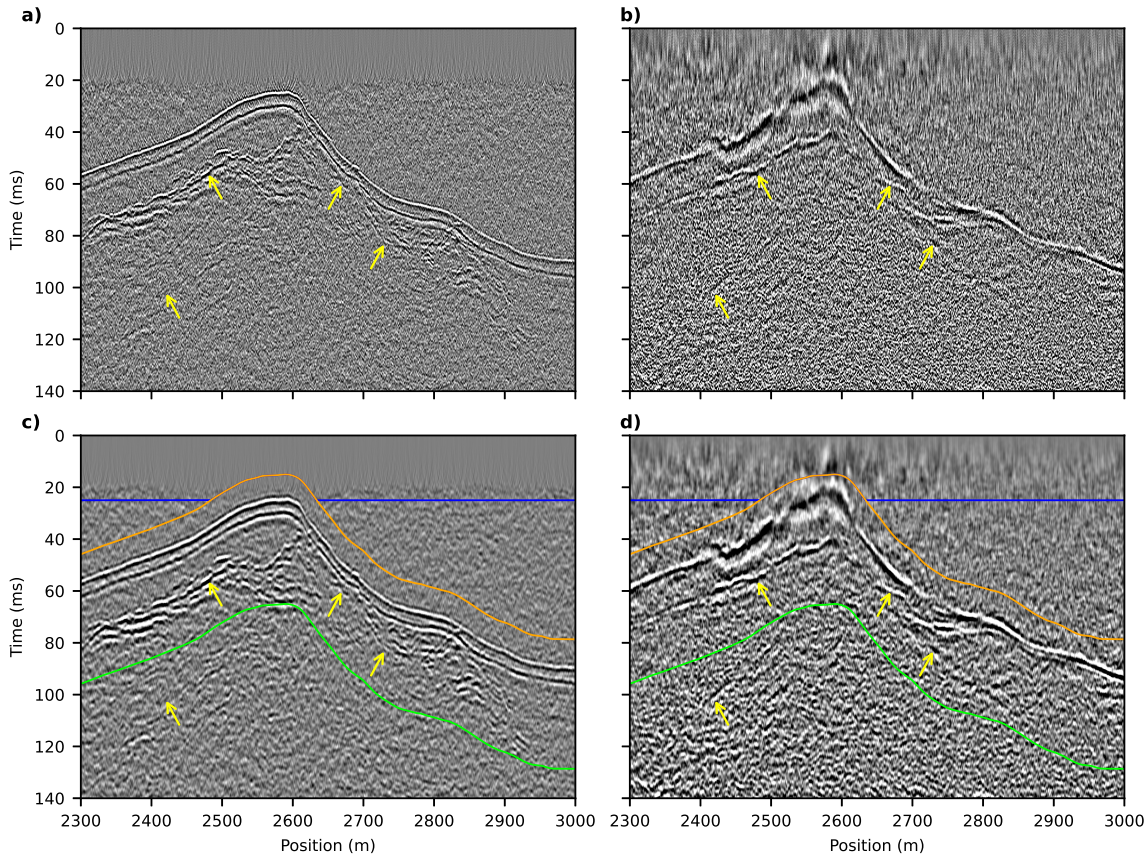

Figure 17: Poststack time migrated seismic images from different data sets: (a) the reference image from a towed single-channel streamer with a 24-element hydrophone array of 7 m active length, (b) the image from seabed DAS with 4 m gauge length, (c) the image of (a) with additional signal enhancement applied, and (d) the image of (b) with the same enhancement applied. The seismic events associated with the water bottom and subsurface reflections are presented in both images. Subsurface reflections in DAS image are highlighted by yellow arrows in comparison with the reference image. The horizontal axis is the distance along the cable. The horizons plotted in (c) and (d) define the signal and noise windows for computing the S/N and spectrum in Figure 20. Signal window is defined between orange and green horizons, whereas noise window is defined between blue and orange horizons.

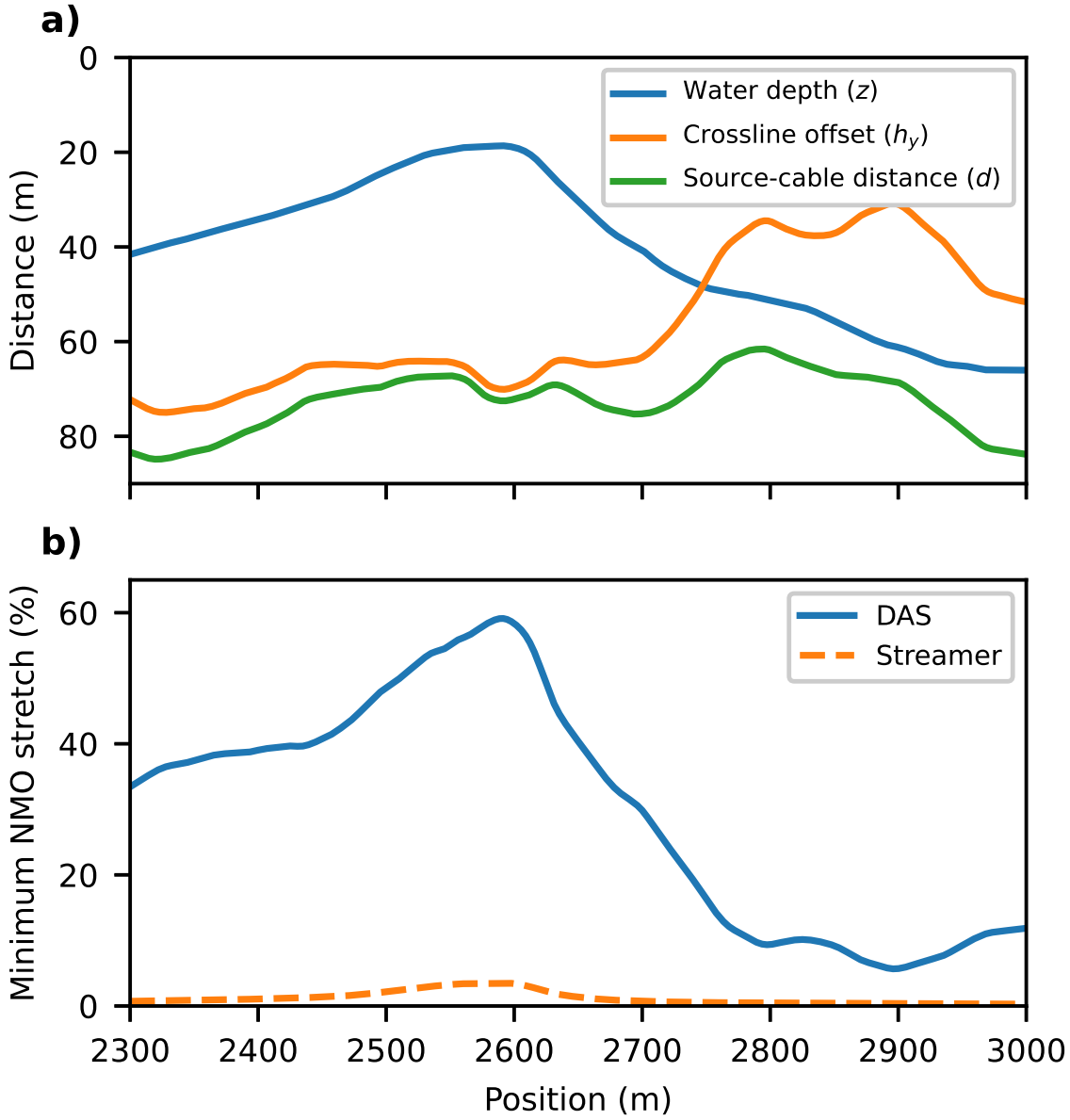

Figure 18: Plots of the following variables at different positions along DAS cable: (a) the water depth (blue), the crossline horizontal offset from source to the DAS cable (orange), the distance between source and the DAS cable (green); and, (b) the minimum NMO stretch associated with the water bottom events in DAS data (solid blue line) and towed streamer data (dashed orange line).

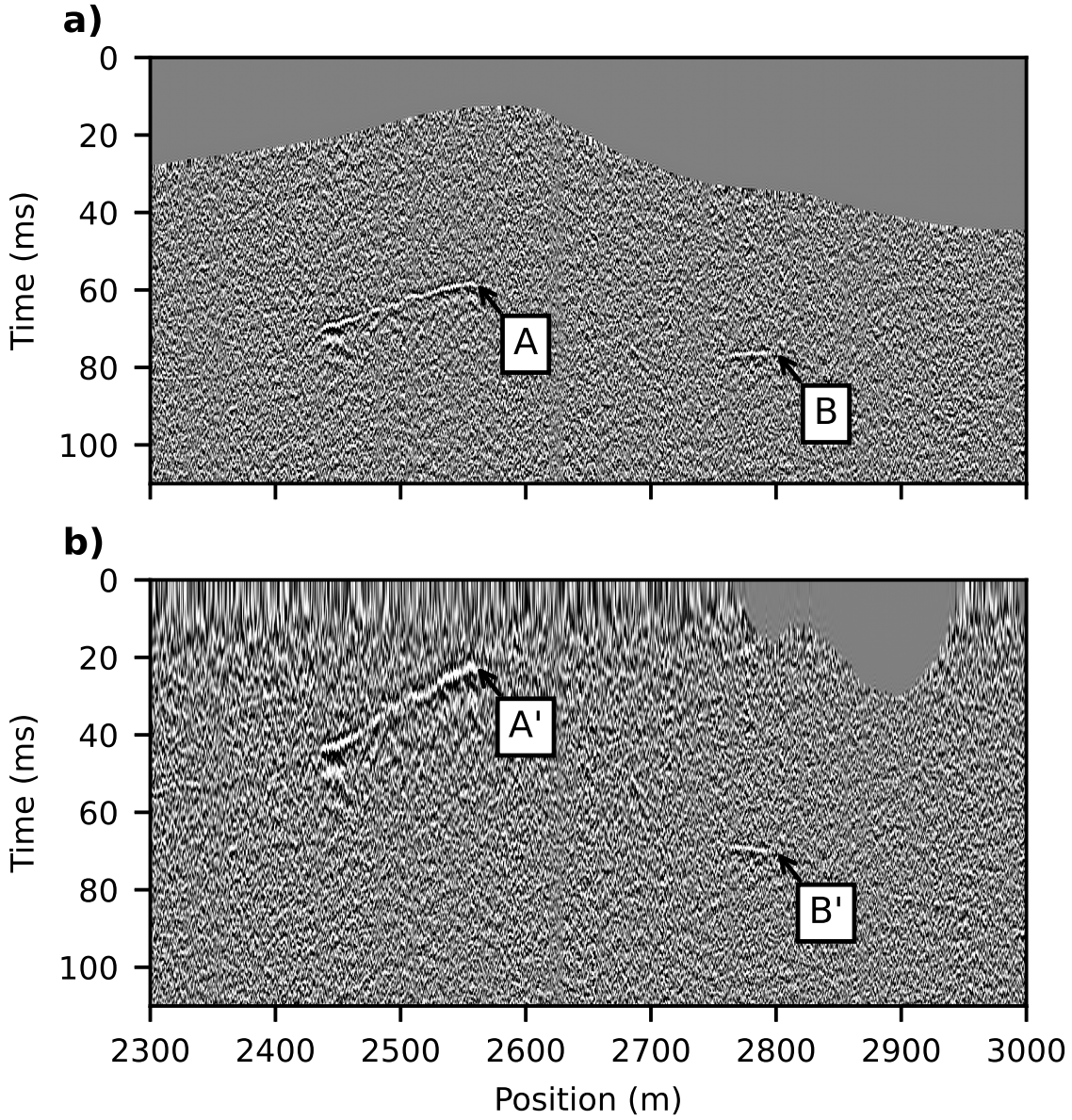

Figure 19: Illustration of NMO stretch effect on a near trace gather of DAS data where sources and receivers are redatumed to the sea surface: (a) near trace gather from the DAS data with common inline offset, and (b) the same gather after NMO correction for the direct wave is applied. The black arrows indicate the two events before and after NMO correction as described in the texts.

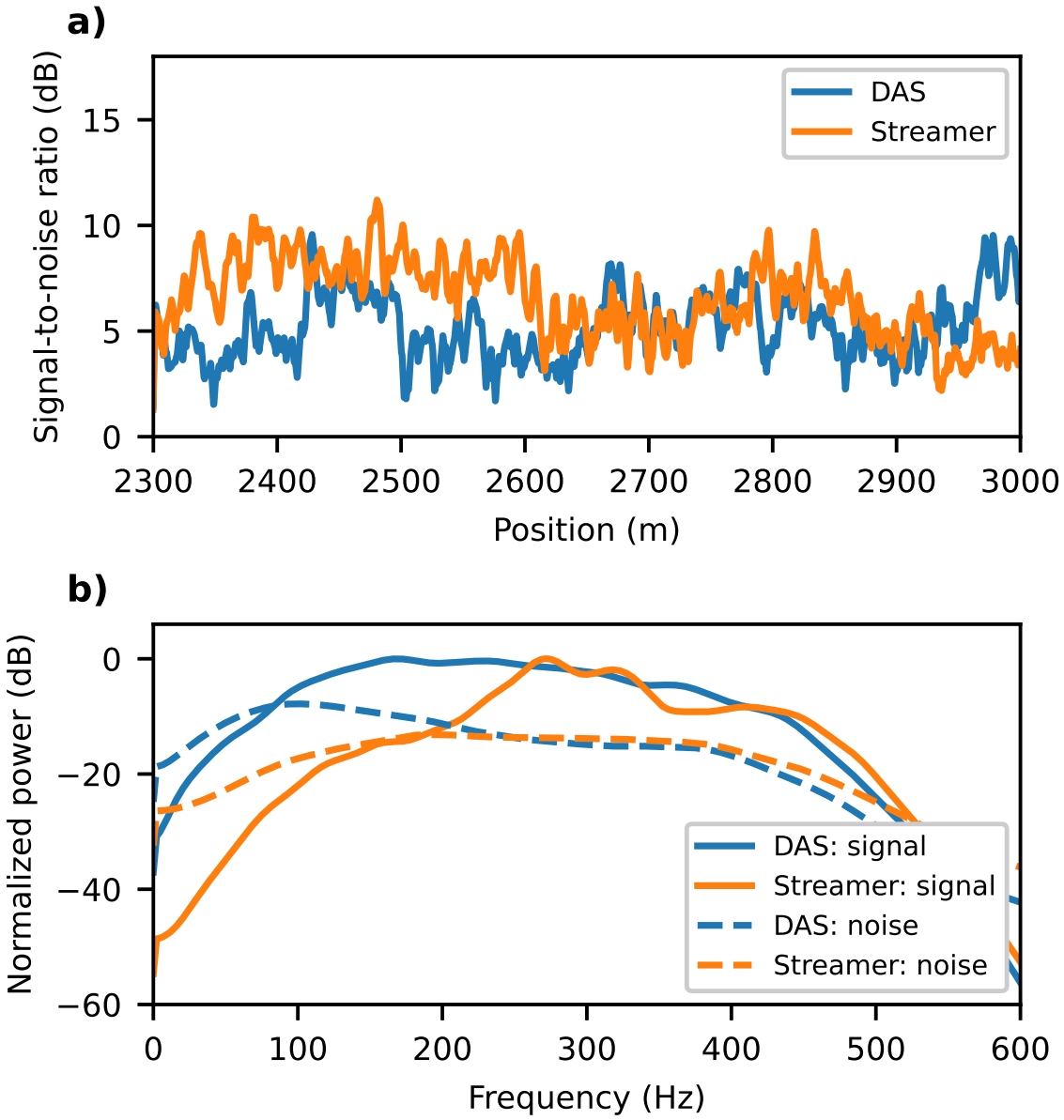

Figure 20: QC plots corresponding to the seismic images from DAS (blue) and towed streamer (orange) with additional signal enhancement applied as shown in Figures 17c and 17d: (a) S/N at different seismic traces, and (b) normalized amplitude spectra within the signal and noise windows. Signal window is defined between orange and green horizons, whereas noise window is defined between the blue and orange horizons in Figure 17.